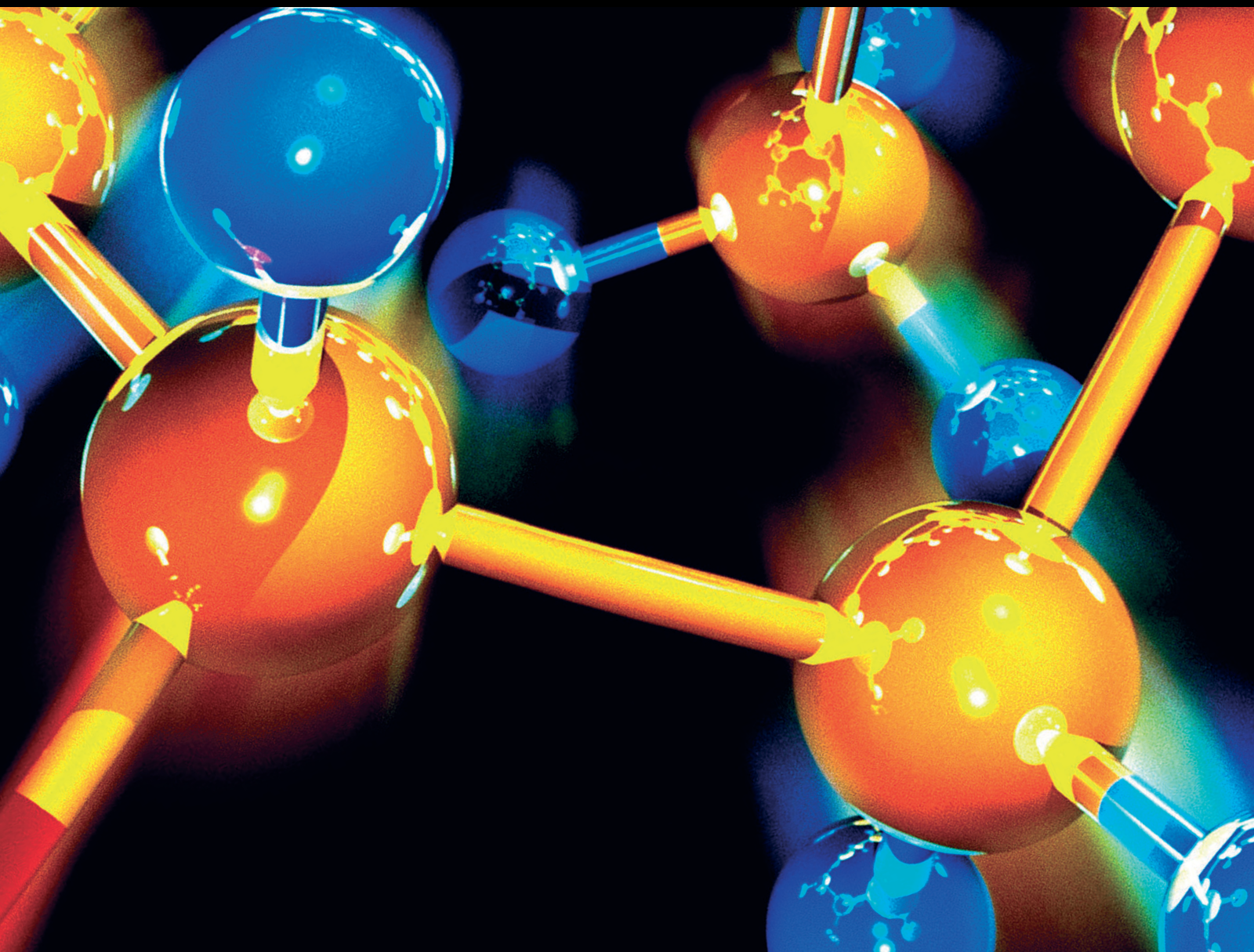# Advances in Photo and Electrical Chemistry for Treatment of Pollutants

Lead Guest Editor: Fada Feng
Guest Editors: Yifan Huang, Haibao Huang, Carlos A. Martínez-Huitle, and Mehrab Mehrvar

Advances in Photo and Electrical Chemistry for Treatment of Pollutants

Advances in Photo and Electrical Chemistry for Treatment of Pollutants

Lead Guest Editor: Fada Feng
Guest Editors: Yifan Huang, Haibao Huang, Carlos
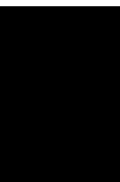A. Martínez-Huitle, and Mehrab Mehrvar

Chief Editor

Kaustubha Mohanty, India

Associate Editors

Mohammad Al-Ghouti, Qatar
Tingyue Gu (iD), USA
Teodorico C. Ramalho (iD), Brazil
Artur M. S. Silva (iD), Portugal

Contents

Research Article

Degradation Pattern of Textile Effluent by Using Bio and Sono Chemical Reactor

Basem Mohammed Al-Sakkaf [ID],[1] **Sadia Nasreen** [ID],[2] **and Naeem Ejaz**[1]

[1]*Department of Civil Engineering, University of Engineering and Technology, Taxila 47080, Pakistan*
[2]*Department of Environmental Engineering, University of Engineering and Technology, Taxila 47080, Pakistan*

Correspondence should be addressed to Sadia Nasreen; sadia.nasreen@uettaxila.edu.pk

The research study was conducted to design the ultrasonic-assisted electrochemical reactor and the bioreactor/filter to evaluate the potential applicability of biological trickling filter system and to compare the efficiency of two reactors such as SER and TF for the treatment of textile industry effluents. Also the study to design Sonoelectrolytic process for wastewater treatment of textile industry containing strong color, high temperature, suspended particles and dissolved solid particles has been conducted. Effect to environment and health is caused by oxygen demand (BOD), high chemical oxygen demand (COD). The percentage removal efficiency for wastewater treatment of textile industry by using sonoelectrolytic reactor (SER) was found to be higher than 95% at temperature of 25°C and a pH value of 8.9, while for trickling filter (TF), having adsorbent as a filter medium, efficiency was found to be 95%, and optimum conditions obtained were applied for the treatment of different dye samples. Based on experimental outcomes, it is determined that treatment through SER is done faster than trickling filter because in TF the adsorbent capacity decreases with time and is a time-consuming process, but the chance of deposition on electrodes also increases in SER, so both these processes can yield better results if these problems are eliminated.

1. Introduction

In the last few years, wastewater from the textile industry has become a big problem which causes an increase in the concentration of environmental pollution in industrial cities, which in turn represents environmental risks [1]. Released wastewater in the textile industry and the chemical dyes can be considered as an important environmental concern, as about 200 L of water is used for every 1 kg of textile production [2]. Textile dyes contain a significant quantity of organic pollutants which are very difficult to degrade, and yearly around 5,000 tons of coloring materials are discharged into our environment [3]. The quantity of used water and the waste production both depend upon the amount of consumed water by several varieties of fabrics, and it changes from one textile industry to another due to reliance on the dyeing process. A rough estimation shows that the bleaching process requires 38% of water, printing

requires 8%, dyeing requires 16%, boiler requires 14%, and 24% is required for additional practices [4]. As a result of diverse processes, an enormous amount of hurtful effluents is discharged to the environment. Thus, textile effluent has a significant bit of colors and further destructive synthetic concoctions that are dangerous to the environment and are a long way from fulfilling the standards.

Textile industry effluent contains large number of harmful agents such as chemical oxygen demand (COD), biological oxygen demand (BOD), suspended particles, dissolved solid particles, chemicals, color and metals (zinc (Zn), arsenic (As), copper (Cu) and, chromium (Cr)) which causes harm to humans and environment [5]. Coloring release contains a composite blend of colors, salts, and further synthetics, for example, surfactants and about 90% of the color and 80% of the salts are released in effluent [6]. Textile effluent is based upon manufacture products and chemicals and is classified in terms of acidic,

basic, vat, and azo dyes while a variety of chemicals inculcated include detergents, caustic, latex, glues, and other chemicals [7]. Textile dyeing works utilizing various classes of chemical dye and extra synthetic substances produceing mixed wastewater [8]. The proficiency of the advanced oxidation process for degrading textile dyes containing the intractable compounds has been comprehensively acknowledged [9–11].

On estimation, most colors utilized in the textile business are effectively solvent in water and are nonbiodegradable due to their unyielding mixes and are a threat to the environment and could cause cancer [12]. The total input of dyes toward wastewater flow is about 15–20% and textile dyeing is contributing about 17%–20% of industrial discharge. There are about 72 toxic chemicals that have been recognized in water from textile dyeing, 30 of which cannot be removed easily [13].

Intense coloration of textile dyes poses high risks to aquatic life by creating obstruction to the light path to reach underwater. Many colors present in fiber effluent potentially cause cancer and mutation and are genotoxic [14]. Material coloring process incorporates different activities, for example, pretreatment, coloring, printing, and washing of pieces of clothing resulting into the generation of a lot of contaminated effluents. The transformation of fiber up to one ton produces about 230–270 cubic meter of polluted water and is required to be cleaned before releasing into the environment [15]. Textile effluents as colors are the most dangerous compound blends found in fiber effluents and ought to be dealt with splendidly as their appearance in water bodies diminishes light invasion, blocking the photosynthesis of watery verdure [16, 17]. Photo-Chemical and ozone chemical treatment processes are collectively resulted as the quick degradation process with better efficiency but the expense of this method is high and is not powerful for treating the entire azo dyes. Also, the generation of various radicals with the expansion of substance reagents causes minor drop of TOC and COD qualities creating the lackluster however degradable polluted water [18].

Industrial dyes involve aromatic compounds in their chemical composition. These dyes are synthesized by chemical combination of altered functional group and relocated electrons. The chromogen comprises a fragrant structure regularly relying upon benzene, naphthalene, or anthracene. The chromophore arrangements are, the azo gathering (-N=N-), ethylene gathering (=C=C=), methine bunch (-CH=), carbonyl gathering (=C=O) and chinoid gatherings. Azo colors might be poisonous after metabolic decrease of the azo bond, creating sweet-smelling amines. The auxo chrome bunches are ionizable gatherings that present coupling limit to the dyematerial. The standard auxo chrome bunches are-NH_2 (amino), -COOH (carboxyl),-SO_3H (sulphonate), and -OH (hydroxyl) [19]. Dyes are classified as natural and synthetic based upon application characteristics and chemical structure. Different treatment techniques of textile wastewater have been proposed in the literature [20].

Fabric industry is perhaps the biggest business on the planet, and various textures, for example, silk, cotton, and fleece are all prerestored, handled, and hued, utilizing a lot of water and a range of chemicals after treatment, so there is a need to comprehend the textile effluent well overall.

1.1. Classification of Dye Removal Techniques. There are several dye removal techniques (Figure 1) which are classified as chemical, physical, and biological methods. Physical method for removing dyes includes adsorption, ion exchange, and filtration/coagulation methods [21, 22], while chemical methods include ozonisation, Fenton reagent, and photocatalytic reactions and biological methods include aerobic degradation, anaerobic degradation, biosorption, etc.

2. Different Technologies Used for This Purpose

2.1. Fenton Oxidation Process. Propelled oxidation strategies, for example, Fenton and altered Fenton forms are impressive to notice dye removal in textilewastewater. In Fenton process, low concentrations of Fe^{+2} and H_2O_2 arrangements are utilized, and these Fenton reagents create OH- radicals including high oxidation potential. The Fenton procedure, where nonlethal and innocuous reagents are applied at low concentrations, is extremely helpful for decolorization of wastewater since it is exceptionally viable and less dirty [23].

2.2. Membrane-Based Technologies. Conventional treatment methods experience the ill effects of a few loopholes. The utilization of film-based procedures in such cases can viably surmount a large portion of these disadvantages. The choice of suitable membrane relies upon the layer material which is thus administered by certain indispensable layer properties, for example, chemical, mechanical thermal and the film defenselessness to fouling; in addition, the layer pore size, which decides the substances that can be adequately held and layer shape, which demonstrates its capability to oppose stopping up are other significant parameters that must be thought about [24, 25]. Microfiltration has constrained application in textile wastewater treatment due to its resemblence with filtration process. It is mainly used for removal of particlessuspension and colloidal dyes from exhausted dye bath and from discarded rinsing bath discharge; microfiltration membranes, however, permit the unconsumed auxiliary chemicals, dissolved organic pollutants and other soluble contaminants to escape with the permeate [25, 26]. The ultrafiltration layer process has restricted applications in the textile business; this is mostly in light of the fact that the subatomic loads of the colors present in the exceptionally hued material release are a lot of lower than the subatomic weight cut-off (MWCO) of the ultrafiltration membranes [27]. Ultrafiltration (UF) is generally applied as a pretreatment step in frameworks requesting high level of procedure stream refinement; it is trailed by procedures, for example, nanofiltration (NF), or
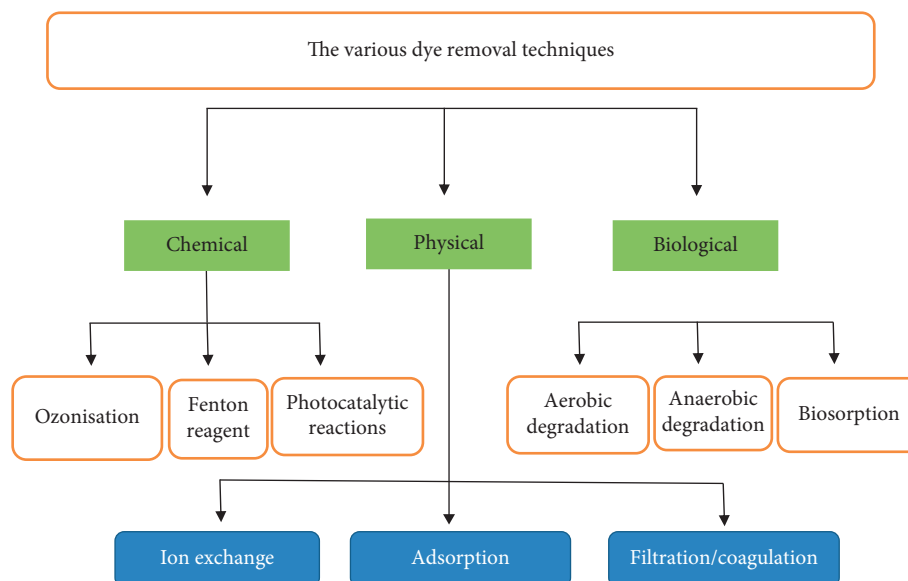
FIGURE 1: Classification of dye removal techniques. Techniques are classified as chemical, physical, and biological methods which are further classified into different techniques.

invert assimilation (RO) stages, which fulfill the requests on process water quality [28]. Nanofiltration (NF) layer process is distinctively put between ultrafiltration and reverse osmosis, Its popularity over the years as an effective and simplified technology can be attributed to the benefits in terms of environmental pollution abatement, rejection, recovery and reuse of textile dyes, divalent salts and other auxiliary chemicals, recovery and reuse of brine . Furthermore, the generation of value pervade permits the reuse of treated wastewaters in significant procedures, for example, coloring and wrapping up [29].

2.3. Adsorption Technique.

Adsorption methods have picked up support methodology among all the physico-chemical techniques including adsorption, flocculation joined with flotation, membrane filtration, electromotor, coagulation, ozonation, oxidation, precipitation, and ion exchange [30, 31]. Activated carbon is a generally utilized adsorbent in modern procedures, which is made out of a miniaturized scale permeable, homogenous structure with high surface territory and shows radiation security [32]. These days, there is an incredible enthusiasm for finding economical and powerful options in contrast to the current business activated carbon [33]. The most recent investigation shows the readiness of activated carbon from coconut husk with H_2SO_4 actuation (CSAC) and its capacity to evacuate textile colors (maxilon blue GRL and direct yellow DY 12) from fluid arrangements [34]. Agricultural wastes are inexhaustible, accessible in huge sums and more affordable when contrasted with different materials utilized as adsorbents. Agricultural squanders are superior to different adsorbents in light of the fact that the horticultural squanders are typically utilized without or with at least handling (washing, drying, and granulating) treatment[35]. There are explicit option farming

by-products utilized strongly as color adsorbents, for example, nut structure, coir essence, and rice husk [36].

2.4. Microbial Biotechnology.

Biotechnological methodologies have pulled in overall consideration for their relative cost viability and ecologically well-disposed nature. Most biotechnological approaches depend on the utilization of organisms that can possibly enzymatically debase and decolorize color containing fiber effluents. Azo dyes have been seen as decolorized prevalently under anaerobic conditions. Complete deterioration of azo dyes by microbial cells happens in two stages. In the initial step, drab metabolites are delivered by the reductive cleavage of the azo bond under anaerobic conditions. These metabolites are then disintegrated in a second step that requires oxidized conditions [37]. Enzymes, for example, azo reductases, laccases, lignin peroxidases, Mn peroxidases, DCIP-NADH reductases, tyrosinase, aminopyrine N-demethylase, and riboflavin reductases, have been accounted for to be engaged with the breakdown of azo dyes [36, 38, 39].

2.5. Ozonation.

Biotreated fabric wastewater can be more dangerous than the untreated discharge as certain colors are changed into little natural atoms; in this manner, further treatment is mostly required. Especially encouraging are the advance oxidation forms (AOPs); among the few AOP ozonation is the innovation that can be effectively executed in the previously existing treatment plants.operate[40, 41]. Utilization of ozonation as short posttreatment after a natural procedure can be gainful for the breakdown of refractory mixes and the evacuation of poisonous quality of material wastewater, yet observing of mutagenicity and harmfulness is a significant apparatus and ought to be utilized to supplement ordinary examination which centers around expulsion of supplements [42].

2.6. Phytoremediation. Phytoremediation really is the technique for treatment of contaminations by plants and their root related microflora [43]. Phytoremediation approach has been examined as a potential instrument to evacuate numerous risky natural contaminants like substantial metals, landfill leachates, pesticides, polyaromatic hydrocarbons, radionuclides, oil, unrefined petroleum, chlorinated solvents, polychlorinated biphenyls, explosives, weapons, and even the harmful gases [44]. Phytoremediation has advantages such as being a solar energy dependent and an aesthetically pleasant method of treatment. It offers a carbon neutral and thus environmental friendly approach for removal of toxic contaminants from the environment [45].

3. Materials and Methods

3.1. Instruments

3.1.1. pH Meter. pH meter is used for the measurement of acidity and alkalinity of solution. pH meter is used to measure the pH of wastewater at different time intervals during wastewater treatment process of industrial dye. This device is also considered as one of the easiest and devices used to measure pH; in addition, this device is equipped with standard solutions to ensure the inspection process for accurate results.

3.1.2. UV-Visible Spectrophotometer. UV-visible spectrophotometer works on the absorption principle. It uses visible light as a source light. Different constituents absorb different wavelengths of visible light. Component concentration has a direct relation with the absorption of light.

Spectrophotometer was used to determine the concentration of dyes in wastewater at different time intervals during treatment process, and it can be explained by using a chart diagram.

3.1.3. Electrolytic Cell. Electrolytic cell is an undivided cell made of Perspex sheet in which degradation was carried out. Working electrode (anode) was made of copper and counter electrode (cathode) was made of aluminum plated iron. Both electrodes had dimensions of $15 \times 4 \, cm^2$ placed vertically at distance of 10 cm to each other.

3.1.4. Ultrasonic Bath. Ultrasonic bath as shown in Figure 2 produces high energy sound waves. The frequency of these waves ranges from 10–400 kHz. These sound waves help in wastewater treatment as they transfer their energy to pollutant molecule. Due to their high energy, the pollutant molecule ruptured.

3.1.5. Sonoelectrolytic Reactor (SER). It is the combination of two units, i.e., an electrolytic cell and ultrasonic bath. The electrolytic cell was placed in the ultrasonic bath, and both are operated simultaneously for wastewater treatment as explained in Figure 2.
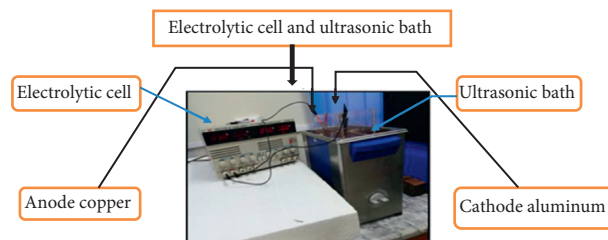

FIGURE 2: Sonoelectrolytic reactor. It is a combination of electrolytic cell and ultrasonic bath.

4. Experimentation

The wastewater was treated with two systems. The experimentation of our study consists of three steps:

(1) Sonoelectrolytic reactor.
(2) Adsorbent use.
(3) Trickling filter.

4.1. Treatment through Sonoelectrolytic Reactor (SER)

4.1.1. Experiment No. 1. 50 ppm concentration of solution of dye colored red was prepared. The volume of solution was 2 L. The underlying pH, temperature, and absorbance were noted, and the arrangement was placed in sonoelectrolytic reactor. The treatment process continued for 210 minutes. The time interval was 30 minutes. Different parameters like absorbance, pH, and temperature were determined after every 30 min of interval.

4.1.2. Experiment No. 2 (Acidic Solution). 50 ppm concentration of red dye solution was prepared. One milliliter for each liter of concentrated HCl was incorporated to solution. Solution's color was changed from red to blue. The absorbance was now measured at wavelength of 570 nm. The volume of solution was 2 L. The initial pH, temperature, and absorbance were noted, and same procedure is repeated as discussed earlier.

4.1.3. Experiment No. 3 (Basic Solution). 50 ppm concentration of red dye solution was prepared. 0.1 N solution NaOH was added to solution. The absorbance was measured at wavelength of 495 nm. The volume of solution was 2 L. The initial pH, temperature, and absorbance were noted, and same procedure is repeated as discussed earlier.

4.1.4. Experiment No. 4 (Acid and Base). 50 ppm concentration of red dye solution was prepared. 0.1 N solution of NaOH and 1 ml/liter of concentrated HCl was added to solution. Agglomerate was formed in the solution. The solution was set for settling. No treatment was done.

4.1.5. Experiment No. 5 (Collected Sample). The sample was collected from cloth dyeing factory. The maximum absorbance that was measured by spectrophotometer was 675 nm. The volume of solution was 1 L. The initial pH, temperature,

and absorbance were noted, and same procedure is repeated as discussed earlier.

4.2. Treatment through Adsorbent

4.2.1. Adsorbent. The adsorbent used was sugarcane bagasse. The sugarcane leftover was collected from sugarcane juice shop and then dried in sunlight and ground into small size.

4.3. Bio-Trickling Filter (TF). The bagasse adsorbent was used in the trickling filter. The laboratory scale trickling filter was constructed as shown in Figure 3. The volume of trickling filter was 4 liters. The filter media used were gravels and adsorbent layer. The filter depth was 8 cm. The bottom layer of filter was of gravels of 10 mm; this layer was of 5 cm. The second layer of 3 cm was laid of gravels having size of 2 mm. The upper layer of adsorbent was thin, approximately 2 mm. The quantity of adsorbent used was 24 gm. Two tests were performed on trickling filter.

4.3.1. Experiment No. 1. 50 ppm concentration of solution of dye colored red was prepared. Volume of suspension was 4 L. The initial pH, temperature, and absorbance were noted, and same procedure is repeated as discussed earlier.

4.3.2. Experiment No. 2 (Collected Sample). The sample was collected from cloth dyeing shop. The maximum absorbance that was measured by spectrophotometer was 675 nm. The volume of solution was 4 L. The initial pH, temperature, and absorbance were noted, and same procedure is repeated as discussed earlier.

5. Results and Discussion

5.1. Treatment through Sonoelectrochemical Reactor

5.1.1. Experiment No. 1. Results shown in Table 1 are explained with the help of graphs (Figure 4(a)–4(c)). Table 1 shows the experiment implementation time and specified 210 minutes, where 8 samples were taken during different time every 30 minutes; the results showed (Figures 4(a)–4(c)) a decrease in the absorbance from 1.637 to 0.413 with an increase in the efficiency from 12.6% up to 99.3% at 210 minutes and equivalent pH values, which means that the processing time is 3.5 hours.

Test continued for 210 minutes and 60 minutes settling was given as shown in Table 1. reactor. The pH also changes during treatment process. The max temperature reaches 61.5°C due to dye degradation because sound waves are highly energetic when they strike with atoms; the atoms are split into small particles which settle down during settling. Similarly, during electrolysis, movement of electrons also degrades dye atoms and emits energy due to this temperature increase. The efficiency was 99.3% after filtration as shown in Table 1.

5.1.2. Experiment No. 2 (Acidic Solution). Table 2 shows the experiment implementation time and specified 90 minutes,

FIGURE 3: Trickling filter. It consists of gravels layer, electrolytic cell, and anode and cathode.

where 4 samples were taken during different time every 30 minutes; the results showed (Figure 5(a)–5(c)) a decrease in the absorbance from 1.154 to 0.059 with an increase in the efficiency from 13.7% up to 94.9% at 90 minutes, which means that the processing time is 1.5 hours.

Test continued for 90 minutes and 60 minutes ettling time was provided.reactorDecrease in absorbance with time depicts the degradation of dye in solution within the reactor. The pH also changes during treatment process. The max temperature reaches 51°C. The efficiency was 94.9% after filtration.

5.1.3. Experiment No. 3 (Basic Solution). Table 3 shows the experiment implementation time and specified 210 minutes, where 4 samples were taken during different time every 30 minutes; the results showed (Figures 6(a)–6(c)) a decrease in the absorbance from 1.548 to 0.074 with an increase in the efficiency from 47.9% up to 95.2% at 210 minutes and high pH values, which means that the processing time is 1.5 hours.

Test continued for 90 minutes and 60 minutes settling was provided. reactorDecrease in absorbance with time depicts the degradation of dye in solution within the reactor. The pH also changes during treatment process. The max temperature reaches 52°C. The efficiency was 95.22% after filtration.

5.1.4. Experiment No. 4 (Collected Sample). Table 4 shows the experiment implementation time and specified 210 minutes, where 4 samples were taken during different time every 30 minutes; the results showed (Figures 7(a)–7(c)) a decrease in the absorbance from 3.824 to 0.138 with an increase in the efficiency from 1.15% up to 96.4% at 210 minutes, which means that the processing time is 1.5 hours.

Test continued for 90 minutes and 60 minutes settling time was provided.reactorDecrease in absorbance with time depicts the degradation of dye in solution within the reactor. The pH also changes during treatment process. The max temperature reaches 59°C. The efficiency was 96.4% after filtration.

Figure 8 shows the initial and final absorbance of wastewater. This shows that SER is a preferable treatment process in short time period.

5.2. Drawbacks of Sonoelectrochemical Reactor. The treatment efficiency of sonoelectrolytic reactor was very good.

TABLE 1: Different characteristic values of red dye in the absence of acid and base.

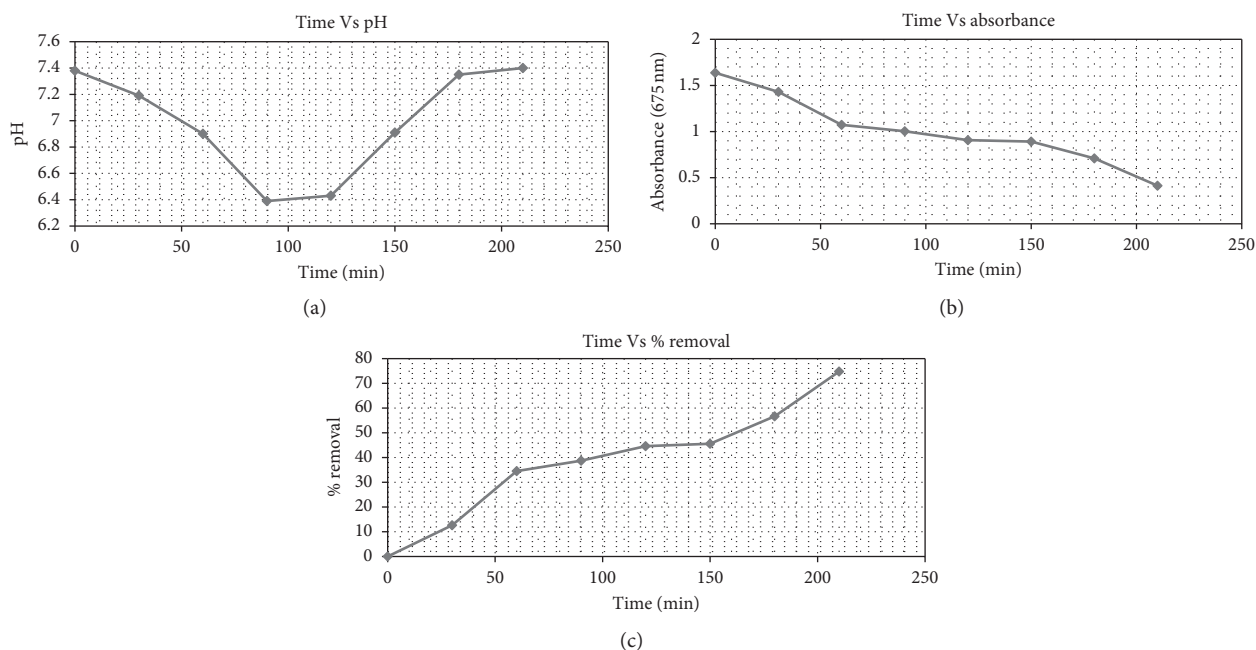| Time (min)	Absorbance (675 nm)	pH	Concentration (ppm)	Removal (%)	Temperature (°C)
0	1.637	7.38	50	0	25
30	1.43	7.19	43.68	12.6	41
60	1.072	6.9	32.74	34.5	47
90	1.003	6.39	30.64	38.7	51
120	0.907	6.43	27.7	44.6	56
150	0.891	6.91	27.21	45.6	58
180	0.709	7.35	21.66	56.7	61
210	0.413	7.4	12.61	74.8	61.2
Settling (60 minutes)	0.091	6.23	2.779	94.4	25
Filtration	0.012	6.45	0.367	99.3	25

(a)

(b)

(c)

FIGURE 4: (a) Plot of pH with respect to time over 250 min period. (b) Plot of absorbance with respect to time over 250 min period. (c) Plot of percent removal with respect to time over 250 min period.

TABLE 2: Different characteristic values of red dye in acidic solution.

Time (min)	Absorbance (675 nm)	pH	Concentration (ppm)	Removal (%)	Temperature (°C)
0	1.154	2.38	50	0	25
30	0.996	2.18	43.2	13.7	42
60	0.413	2.15	17.9	64.2	45
90	0.308	2.45	13.3	73.3	51
Settling (60 minutes)	0.101	4.85	4.38	91.2	25
Filtration	0.059	5.02	2.56	94.9	25

The only drawback assessed was deposition of dyes on electrodes during the treatment process that needs cleaning after every test. This depends upon the concentration of dyes in wastewater; higher concentration leads toward more deposition on electrodes. Another problem which may occur was sludge formation. High amount of sludge is produced in this process that is difficult to handle.

5.3. Treatment through Bio-Trickling Filter (TF)

5.3.1. Experiment No. 1. Table 5 shows the experiment implementation time and specified 110 minutes, where 4 samples were taken during different time every 30 minutes; the results showed (Figures 9(a)–9(c)) a decrease in the absorbance from 1.591 to 0.067 with an increase in the
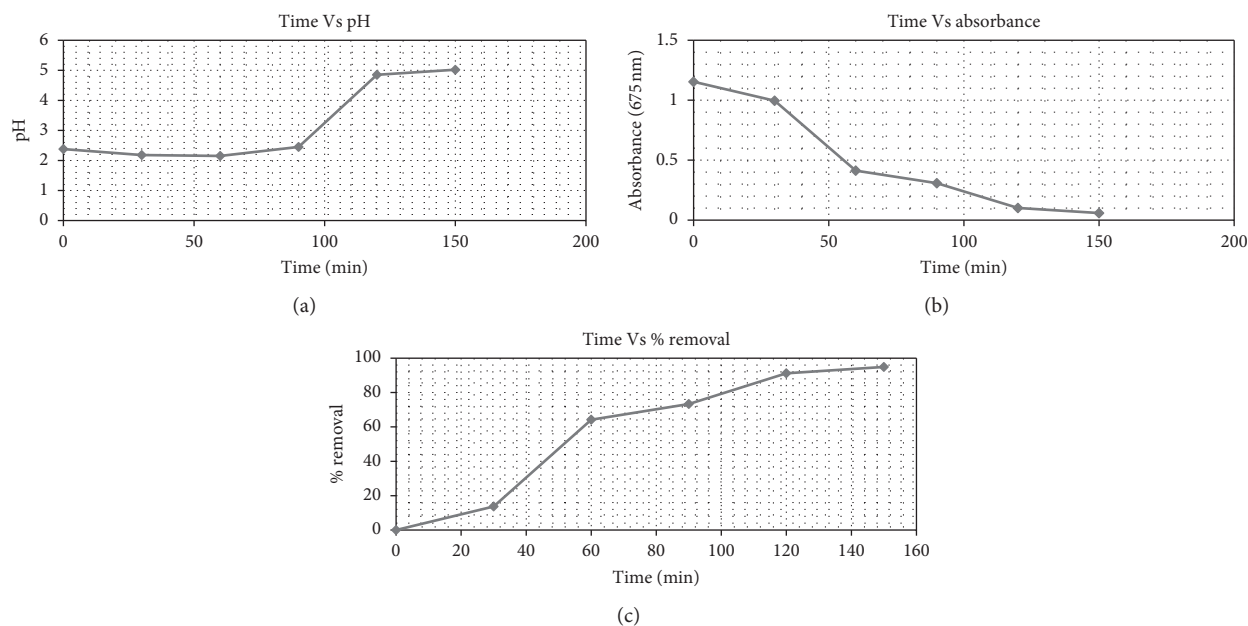
(a)

(b)

(c)

FIGURE 5: (a) Plot of pH with respect to time over 200 min period. (b) Plot of absorbance with respect to time over 200 min period. (c) Plot of percent removal with respect to time over 160 min period.

TABLE 3: Different characteristic values of red dye in basic solution.

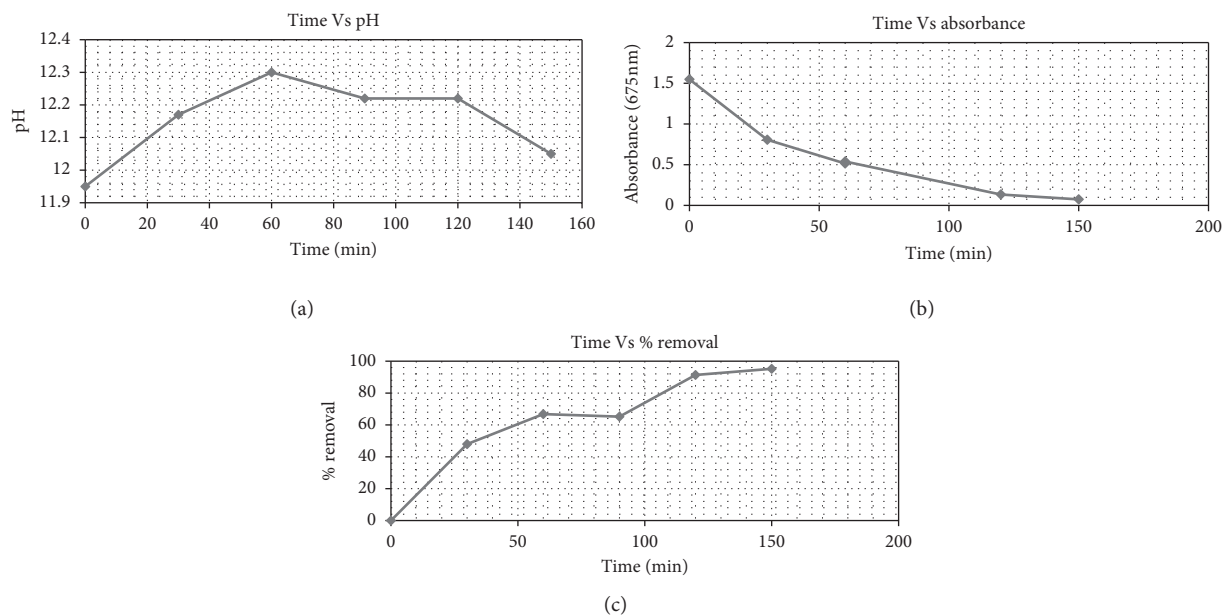| Time (min)	Absorbance (675 nm)	pH	Concentration (ppm)	Removal (%)	Temperature (°C)
0	1.548	11.95	50	0	25
30	0.806	12.17	26	47.93	41
60	0.514	12.3	16.6	66.8	45
90	0.539	12.22	17.4	65.18	52
Settling (60 minutes)	0.134	12.22	4.33	91.34	25
Filtration	0.074	12.05	2.39	95.22	25

(a)

(b)

(c)

FIGURE 6: (a) Plot of pH with respect to time over 160 min period. (b) Plot of absorbance with respect to time over 200 min period. (c) Plot of percent removal with respect to time over 200 min period.

TABLE 4: Different characteristic values of collected sample.

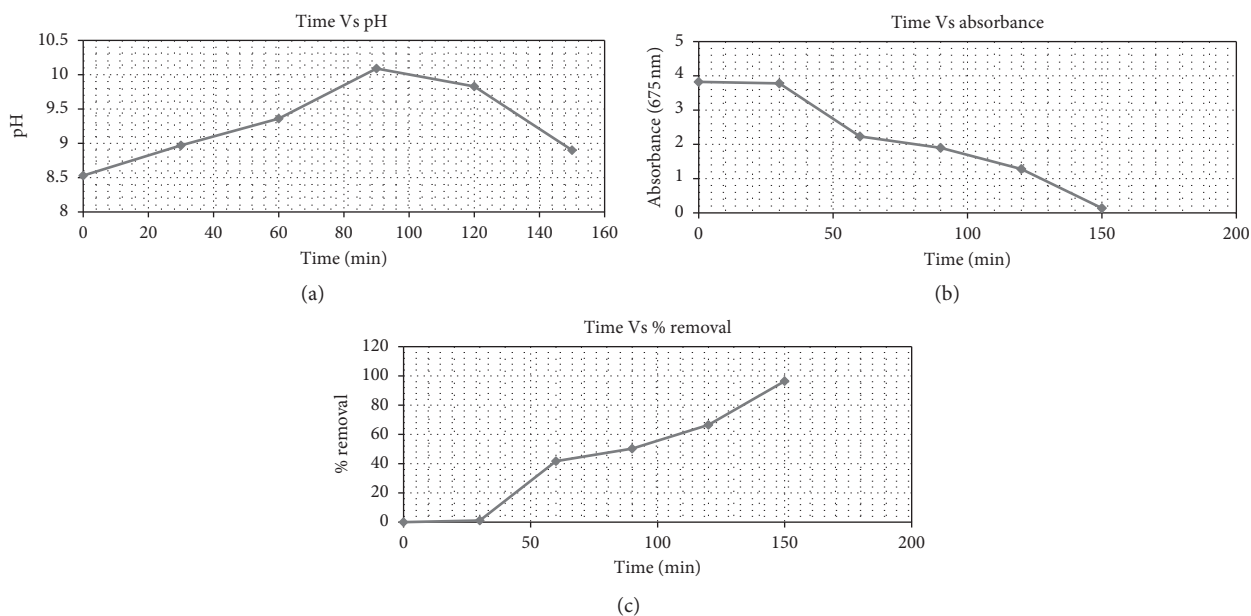| Time (min)	Absorbance (675 nm)	pH	Removal (%)	Temperature (°C)
0	3.824	8.53	0	25
30	3.78	8.97	1.15	47
60	2.23	9.36	41.7	55
90	1.9	10.09	50.3	59
Settling (60 minutes)	1.28	9.83	66.5	25
Filtration	0.138	8.9	96.4	25

(a)

(b)

(c)

FIGURE 7: (a) Plot of pH with respect to time over 160 min period. (b) Plot of absorbance with respect to time over 200 min period. (c) Plot of percent removal with respect to time over 200 min period.
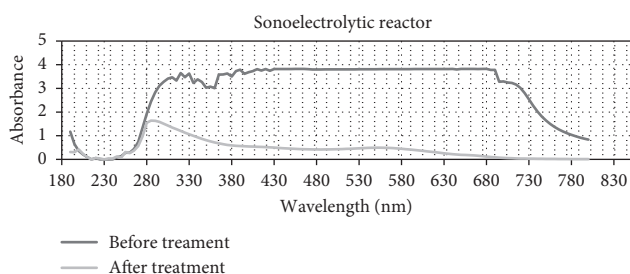

FIGURE 8: Plot of absorbance with respect to wavelength over 830 nm. It shows a change in parameters of wastewater (before and after treatment).

efficiency from 83.47% up to 95.78% at 110 minutes and equivalent pH values, which means that the processing time is 1.5 hours.

Test continued for 110 minutes. reactorDecrease in absorbance with time depicts the degradation of dye in solution within the reactor. The pH also changes during treatment process. The efficiency was 95.8%.

5.3.2. Experiment No. 2 (Collected Sample). Table 6 shows the experiment implementation time and specified 240 minutes, where 9 samples were taken during different time every 30 minutes; the results showed (Figures 10(a)–10(c)) a decrease in the absorbance from 3.79 to 2.02 with an increase in the efficiency from 20.95% up to 46.7% at 240 minutes and equivalent pH values, which means that the processing time is 4 hours.

Test continued for 110 minutes. reactorDecrease in absorbance with time depicts the degradation of dye in solution within the reactor. The pH also changes during treatment process. The efficiency was 46.7%.

The graph in Figure 11 shows the initial and final absorbance of wastewater. This shows that TF is not a good treatment process in short time period. Also the graph shows abrupt variation causing an increase in absorbance value as reaction stopped and particles deposited instead of settling deposited. The problem can be removed using filter paper.

5.4. Drawbacks of Bio-Trickling Filter. Treatment in bio-trickling filter is a time-consuming process as both the

TABLE 5: Different characteristic values as a result of dye treatment through biofilter.

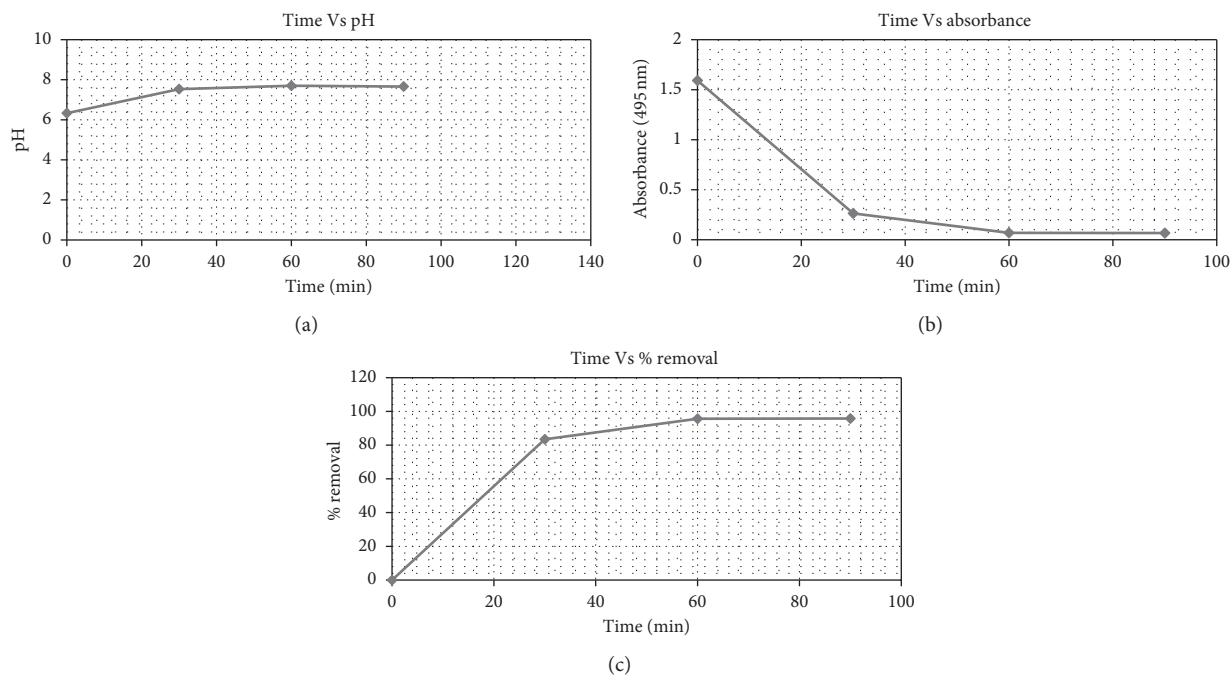| Time (min)	Absorbance (495 nm)	pH	Concentration (ppm)	Removal (%)
0	1.591	6.33	50	0
30	0.263	7.53	8.27	83.47
90	0.069	7.7	2.17	95.663
110	0.067	7.66	2.11	95.789

(a)

(b)

(c)

FIGURE 9: (a) Plot of pH with respect to time over 140 min period. (b) Plot of absorbance with respect to time over 100 min period. (c) Plot of percent removal with respect to time over 100 min period.

TABLE 6: Different characteristic values of collected sample treatment through biofilter.

Time (min)	Absorbance (495 nm)	pH	Removal (%)
0	3.79	7.38	0
60	2.966	7.74	20.95
120	2.413	7.75	36.332
180	2.182	7.73	42.427
240	2.02	7.6	46.702

biological treatment and the physical treatment are required. Biofilm generation is a time requisite process, and the other issue was the capacity of adsorbent. The adsorbent capacity decreases with time, and when adsorbent surface area is utilized thoroughly, there is a need to replace the old adsorbent with the new one.

5.5. Comparative Analysis of Both Treatment Systems. Table 7 shows the comparative analysis of treatment systems by sonoelectrolytic reactor and trickling filter.

5.6. Efficiency Comparison of Both Treatment Systems. Figure 12 shows the relevance between treatment efficiencies and time. It shows that sonoelectrolytic reactor (SER) took

less time to treat textile wastewater as compared to trickling filter.

5.7. Effect of Temperature. Figures 13(a) and 13(b) show the temperature variation with respect to time for different experimental setup used in the ultrasound-assisted electrochemical reactor (UAER) method. It is observed that temperature increases as the experiment progresses. The absorbance decreases with increase of temperature, ultimately causing dye degradation to increase, respectively. The maximum temperature noted in UAER method is 56°C.

Figure 13(b) shows the temperature variation for different experimental setup used in the sonoelectrochemical reactor (SER) method. The temperature shows the similar effect as observed in UEAR graph values. The maximum temperature noted in the SER method is 59°C. After 90 minutes, the experiment stops and the aqueous solution is kept for settling for 60 minutes, causing an abrupt decrease of temperature. Also, it is noted in both UEAR and SER methods that the rate of decolonization reduces after temperature reaches 50°C and rate of increase of temperature also decreases after 150 minutes in both the aforementioned techniques.

Time Vs pH

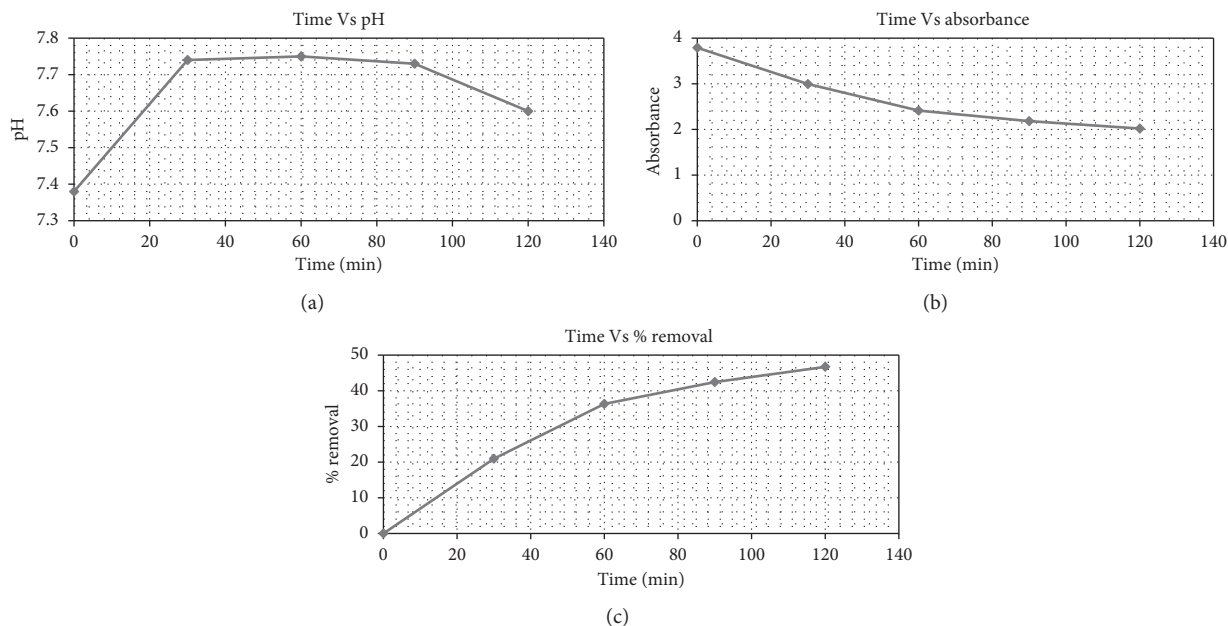Time Vs absorbance

(a)

(b)

Time Vs % removal

(c)

FIGURE 10: (a) Plot of pH with respect to time over 140 min period. (b) Plot of absorbance with respect to time over 140 min period. (c) Plot of percent removal with respect to time over 140 min period.

Trickling filter

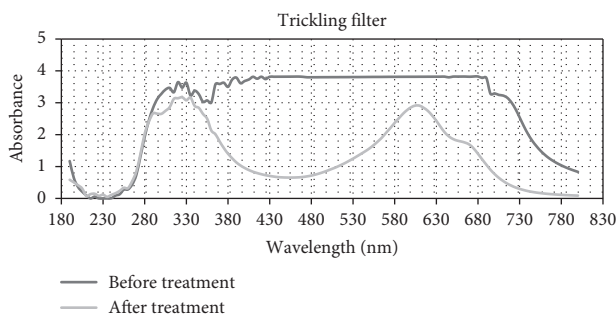—— Before treatment
—— After treatment

FIGURE 11: Plot of absorbance with respect to wavelength over 830 nm. It shows the treatment efficiency of trickling filter.

TABLE 7: Comparative analysis of treatment systems.

Sonoelectrolytic reactor	Trickling filter
Fast treatment process	Slow treatment process
Increased copper concentration in effluent	No increase in copper concentration in effluent
Deposition on electrodes	Adsorbent capacity decreases with process
More efficiency w.r.t time	Less efficient w.r.t time

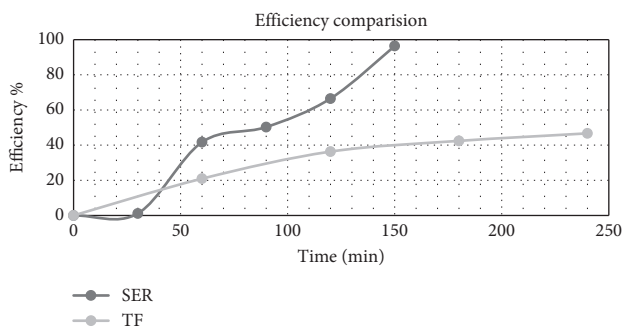Efficiency comparision

—●— SER
—●— TF

FIGURE 12: Plot of efficiency with respect to time over 250 min period. It shows the efficiency comparison of SER and TF.
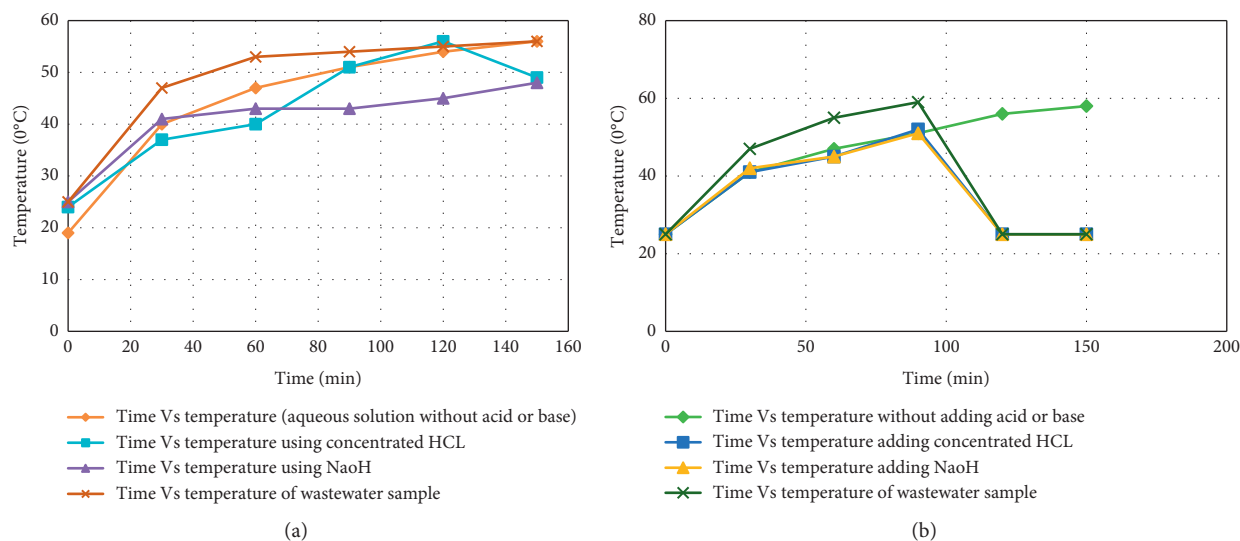
(a)

(b)

FIGURE 13: (a) Temperature variation graph with respect to time using the UEAR method. (b) Temperature variation graph with respect to time using the SER method.
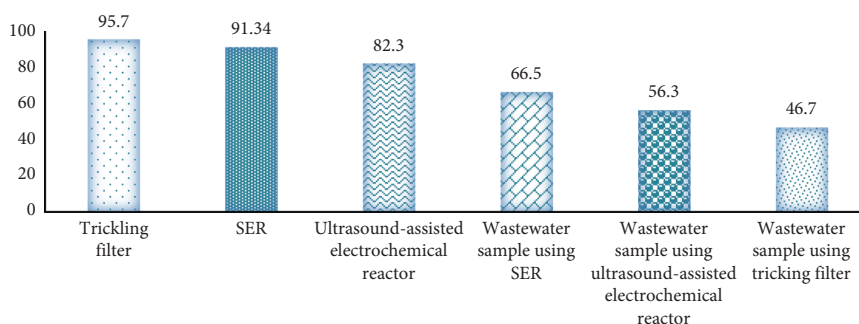

FIGURE 14: Comparison based on efficiency. Dye removal percentage using different techniques.

Figure 14 shows the comparison between trickling filter, sonoelectrolytic reactor, and ultrasound-assisted electrochemical reactor based on their degradation efficiency.

6. Conclusion

Fabric discharge can cause drain, ulceration of skin, sickness, skin bothering, and dermatitis. Excessive quantity of harmful synthetic substances in the wastewater inhibits sunlight and enhances biological oxygen demand, thereby hindering photosynthesis and reoxygenation process. Hence, the need to treat such an effluent is urgent.

In this study, performances of sonoelectrolytic and biological processes to remove color and organic compounds from fabric discharge were investigated and compared. After performing a series of experiments on dye solution, it was easy to conclude that efficiency of degradation of dyes can be enhanced by changing the parameters like pH, temperature, and types of chemicals used. Conclusions derived from the experimental results shows that the treatment through SER is faster than trickling filter because in TF the adsorbent capacity decreases with time and is a time-consuming process, but the chance of deposition on electrodes also increases in SER so both these processes can yield better results if these problems are eliminated.

Data Availability

The data used to support the findings of the study are available from the corresponding author upon request.

Conflicts of Interest

The authors declare that they have no conflicts of interest.

References

[1] S. Rajoriya, S. Bargole, S. George, and V. K. Saharan, "Treatment of textile dyeing industry effluent using hydrodynamic cavitation in combination with advanced oxidation reagents," *Journal of Hazardous Materials*, vol. 344, pp. 1109–1115, 2018.

[2] D. A. Yaseen and M. Scholz, "Textile dye wastewater characteristics and constituents of synthetic effluents: a critical review," *International Journal of Environmental Science and Technology*, vol. 16, no. 2, pp. 1193–1226, 2019.

[3] A. Pirkarami and M. E. Olya, "Removal of dye from industrial wastewater with an emphasis on improving economic efficiency and degradation mechanism," *Journal of Saudi Chemical Society*, vol. 21, pp. S179–S186, 2017.

[4] F. Ntuli, "Characterization of effluent from textile wet finishing operations," in *Proceedings of the World Congress on Engineering and Computer Science., 2009*, London, UK, July 2009.

[5] S. Imtiazuddin, M. Mumtaz, and K. A. Mallick, "Pollutants of wastewater characteristics in textile industries," *Journal of Basic and Applied Sciences*, vol. 8, pp. 554–556, 2012.

[6] X. Lu, L. Liu, R. Liu, and J. Chen, "Textile wastewater reuse as an alternative water source for dyeing and finishing processes: a case study," *Desalination*, vol. 258, no. 1–3, pp. 229–232, 2010.

[7] S. Popli and U. D. Patel, "Destruction of azo dyes by anaerobic-aerobic sequential biological treatment: a review," *International Journal of Environmental Science and Technology*, vol. 12, no. 1, pp. 405–420, 2015.

[8] V. M. Correia, T. Stephenson, and S. J. Judd, "Characterisation of textile wastewaters-a review," *Environmental Technology*, vol. 15, no. 10, pp. 917–929, 1994.

[9] D. S. Babu, V. Srivastava, P. V. Nidheesh, and M. S. Kumar, "Detoxification of water and wastewater by advanced oxidation processes," *Science of the Total Environment*, vol. 696, p. 133961, 2019.

[10] R. Javaid and U. Y. Qazi, "Catalytic oxidation process for the degradation of synthetic dyes: an overview," *International Journal of Environmental Research and Public Health*, vol. 16, no. 11, p. 2066, 2019.

[11] J. Madhavan, J. Theerthagiri, D. Balaji, S. Sunitha, Choi, and M. Ashokkumar, "Hybrid advanced oxidation processes involving ultrasound: an overview," *Molecules*, vol. 24, no. 18, p. 3341, 2019.

[12] A. B. Dos Santos, F. J. Cervantes, and J. B. Van Lier, "Review paper on current technologies for decolourisation of textile wastewaters: perspectives for anaerobic biotechnology," *Bioresource Technology*, vol. 98, no. 12, pp. 2369–2385, 2007.

[13] F. M. D. Chequer, T. M. Lizier, R. de Felício et al., "Analyses of the genotoxic and mutagenic potential of the products formed after the biotransformation of the azo dye Disperse Red 1," *Toxicology in Vitro*, vol. 25, no. 8, pp. 2054–2063, 2011.

[14] R. O. A. de Lima, A. P. Bazo, D. M. F. Salvadori, C. M. Rech, D. d. P. Oliveira, and G. d. A. Umbuzeiro, "Mutagenic and carcinogenic potential of a textile azo dye processing plant effluent that impacts a drinking water source," *Mutation Research/Genetic Toxicology and Environmental Mutagenesis*, vol. 626, no. 1-2, pp. 53–60, 2007.

[15] C. Zaharia, D. Suteu, A. Muresan, R. Muresan, and A. Popescu, "Textile wastewater treatment by homogeneous oxidation with hydrogen peroxide," *Environmental Engineering and Management Journal*, vol. 8, no. 6, pp. 1359–1369, 2009.

[16] E. C. Lima, B. Royer, J. C. P. Vaghetti et al., "Application of Brazilian pine-fruit shell as a biosorbent to removal of reactive red 194 textile dye from aqueous solution," *Journal of Hazardous Materials*, vol. 155, no. 3, pp. 536–550, 2008.

[17] B. Royer et al., "Applications of Brazilian pine-fruit shell in natural and carbonized forms as adsorbents to removal of methylene blue from aqueous solutions—kinetic and equilibrium study," *Journal of Hazardous Materials*, vol. 164, no. 2-3, pp. 1213–1222, 2009.

[18] A. Sakalis, K. Fytianos, U. Nickel, and A. Voulgaropoulos, "A comparative study of platinised titanium and niobe/synthetic diamond as anodes in the electrochemical treatment of textile wastewater," *Chemical Engineering Journal*, vol. 119, no. 2-3, pp. 127–133, 2006.

[19] A. Gürses, "Dyes and pigments: their structure and properties," in *Dyes and Pigments*, pp. 13–29, Springer, Berlin, Germany, 2016.

[20] V. Golob, A. Vinder, and M. Simonic, "Efficiency of the coagulation/flocculation method for the treatment of dyebath effluents," *Dyes and Pigments*, vol. 67, no. 2, pp. 93–97, 2005.

[21] G. Crini and E. Lichtfouse, "Advantages and disadvantages of techniques used for wastewater treatment," *Environmental Chemistry Letters*, vol. 17, no. 1, pp. 145–155, 2019.

[22] K. G. Pavithra, P. Senthil Kumar, V. Jaikumar, and P. Sundar Rajan, "Removal of colorants from wastewater: a review on sources and treatment strategies," *Journal of Industrial and Engineering Chemistry*, vol. 75, pp. 1–19, 2019.

[23] K. Lacasse and W. Baumann, "Environmental considerations for textile processes and chemicals," in *Textile Chemicals*, pp. 484–647, Springer, Berlin, Germany, 2004.

[24] A. B. Koltuniewicz and E. Drioli, "Membranes in clean technologies," *Membranes*, vol. 31, pp. 3–1, 2008.

[25] J. Dasgupta, J. Sikder, S. Chakraborty, S. Curcio, and E. Drioli, "Remediation of textile effluents by membrane based treatment techniques: a state of the art review," *Journal of Environmental Management*, vol. 147, pp. 55–72, 2015.

[26] Y. Juang, E. Nurhayati, C. Huang, J. R. Pan, and S. Huang, "A hybrid electrochemical advanced oxidation/microfiltration system using BDD/Ti anode for acid yellow 36 dye wastewater treatment," *Separation and Purification Technology*, vol. 120, pp. 289–295, 2013.

[27] H. Ouni and M. Dhahbi, "Spectrometric study of crystal violet in presence of polyacrylic acid and polyethylenimine and its removal by polyelectrolyte enhanced ultrafiltration," *Separation and Purification Technology*, vol. 72, no. 3, pp. 340–346, 2010.

[28] S. Barredo-Damas et al., "Application of nanofiltration/reverse osmosis membranes to textile effluents aiming its reclamation and reuse: influence of operating conditions," *Chemical Engineering Transactions*, vol. 21, pp. 1027–1032, 2010.

[29] M. R. Hoffmann, S. T. Martin, W. Choi, and D. W. Bahnemann, "Environmental applications of semiconductor photocatalysis," *Chemical Reviews*, vol. 95, no. 1, pp. 69–96, 1995.

[30] M. Sulak, E. Demirbas, and M. Kobya, "Removal of Astrazon Yellow 7GL from aqueous solutions by adsorption onto wheat bran," *Bioresource Technology*, vol. 98, no. 13, pp. 2590–2598, 2007.

[31] K. Xie, W. Zhao, and X. He, "Adsorption properties of nanocellulose hybrid containing polyhedral oligomeric silsesquioxane and removal of reactive dyes from aqueous solution," *Carbohydrate Polymers*, vol. 83, no. 4, pp. 1516–1520, 2011.

[32] M. J. Iqbal and M. N. Ashiq, "Adsorption of dyes from aqueous solutions on activated charcoal," *Journal of Hazardous Materials*, vol. 139, no. 1, pp. 57–66, 2007.

[33] Z. A. ALOthman, M. Naushad, and R. Ali, "Kinetic, equilibrium isotherm and thermodynamic studies of Cr (VI) adsorption onto low-cost adsorbent developed from peanut shell activated with phosphoric acid," *Environmental Science and Pollution Research*, vol. 20, no. 5, pp. 3351–3365, 2013.

[34] A. M. Aljeboree, A. N. Alshirifi, and A. F. Alkaim, "Kinetics and equilibrium study for the adsorption of textile dyes on coconut shell activated carbon," *Arabian Journal of Chemistry*, vol. 10, pp. S3381–S3393, 2017.

[35] A. S. Franca, L. S. Oliveira, and M. E. Ferreira, "Kinetics and equilibrium studies of methylene blue adsorption by spent coffee grounds," *Desalination*, vol. 249, no. 1, pp. 267–272, 2009.

[36] M. T. Yagub, T. K. Sen, S. Afroze, and H. M. Ang, "Dye and its removal from aqueous solution by adsorption: a review," *Advances in Colloid and Interface Science*, vol. 209, pp. 172–184, 2014.

[37] U. Shedbalkar and J. P. Jadhav, "Detoxification of malachite green and textile industrial effluent by Penicillium ochrochloron," *Biotechnology and Bioprocess Engineering*, vol. 16, no. 1, pp. 196–204, 2011.

[38] T. Hadibarata, A. R. M. Yusoff, A. Aris, Salmiati, T. Hidayat, and R. A. Kristanti, "Decolorization of azo, triphenylmethane and anthraquinone dyes by laccase of a newly isolated armillaria sp. F022," *Water, Air, & Soil Pollution*, vol. 223, no. 3, pp. 1045–1054, 2012.

[39] M. Zheng, Y. Chi, H. Yi, and S. Shao, "Decolorization of Alizarin Red and other synthetic dyes by a recombinant laccase from Pichia pastoris," *Biotechnology Letters*, vol. 36, no. 1, pp. 39–45, 2014.

[40] C. M. Radetski, S. M. C. Rosa, E. V. C. Rosa, M. M. De Souza Sierra, and E. L. Simionatto, "Ozonation of textile wastewater: physico-chemical and phytotoxic aspects," *Environmental Technology*, vol. 23, no. 5, pp. 537–545, 2002.

[41] O. S. G. P. Soares, J. J. M. Órfão, D. Portela, A. Vieira, and M. F. R. Pereira, "Ozonation of textile effluents and dye solutions under continuous operation: influence of operating parameters," *Journal of Hazardous Materials*, vol. 137, no. 3, pp. 1664–1673, 2006.

[42] M. Punzi, F. Nilsson, A. Anbalagan et al., "Combined anaerobic-ozonation process for treatment of textile wastewater: removal of acute toxicity and mutagenicity," *Journal of Hazardous Materials*, vol. 292, pp. 52–60, 2015.

[43] M. Nie, "Understanding plant-microbe interactions for phytoremediation of petroleum-polluted soil," *PLoS One*, vol. 6, no. 3, Article ID e17961, 2011.

[44] C. O. Nwoko, "Trends in phytoremediation of toxic elemental and organic pollutants," *African Journal of Biotechnology*, vol. 9, no. 37, pp. 6010–6016, 2010.

[45] A. C. Dietz and J. L. Schnoor, "Advances in phytoremediation," *Environmental Health Perspectives*, vol. 109, no. 1, pp. 163–168, 2001.

Research Article

Application of Ultraviolet Radiation to Control the Calcium Carbonate Scale Formation and Deposition on the Membranes

Chanbasha Basheer ⬤,[1] **Mokhtar Rashwan,**[1] **Eid Al-Mutairi,**[2] **Amjad A. Shaikh,**[2] **and Khurram Karim Qureshi**[3]

[1]*Department of Chemistry, King Fahd University of Petroleum and Minerals, Dhahran 31261, Saudi Arabia*
[2]*Department of Chemical Engineering, King Fahd University of Petroleum and Minerals, Dhahran 31261, Saudi Arabia*
[3]*Department of Electrical Engineering, King Fahd University of Petroleum and Minerals, Dhahran 31261, Saudi Arabia*

Correspondence should be addressed to Chanbasha Basheer; cbasheer@kfupm.edu.sa

Scale formation on surfaces in contact with water supersaturated with calcium carbonate creates technical problems, including heat transfer hindrance, energy consumption, and equipment shutdown. Thus, nowadays, there is an increasing need for new approaches that are environmentally friendly and economically feasible. In this work, for the first time, calcium carbonate growth was investigated using UV light exposure, and the growth rate was compared with control and commercial antiscalant. Saturated calcium carbonate samples were exposed to UV radiation; the growth rate of calcium carbonate crystals was monitored at different time intervals. Results clearly show that about 85% decrease in crystal growth rate was observed when compared to 43% after the addition of 3 mg/L of amino tris(methylene phosphonic acid) antiscalant. Calcium carbonate scale deposition on hydrophobic and hydrophilic membranes was investigated. The amount of scale deposited in the case of a UV-treated sample is insignificant when compared to control samples. Thus, the exposure of UV might help to improve the membranes' lifetime. X-ray diffraction and scanning electron microscopy analyses revealed that UV light treatment produced mostly calcite crystals. The produced calcites are less dense and less adherent, and it can be easily removable when compared to other types of calcium carbonate phases. Thus, UV radiation is an efficient green approach for calcium carbonate scale mitigation on membrane surfaces.

1. Introduction

Calcium carbonate scale formation is a major challenge in the transportation and operational oil pipelines in oil industries. The risk of scale deposition occurs during the course of injection operations mostly because of change in temperature that aid solution rapid supersaturation, the process that encourages the decomposition of HCO_3^- according to the following reaction:

$$2HCO_3^- (aq) = CO_3^{2-} (aq) + CO_2 (aq) + H_2O \qquad (1)$$
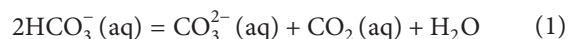
The mineral scale can also be formed from the reaction of two chemicals that lead to precipitation:

$$CO_3^{2-} (aq) + Ca^{2+} (aq) = CaCO_3 (s) \qquad (2)$$
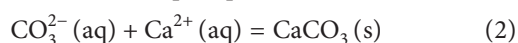
The calcite crystals are large, but, in the presence of impurities, they take the form of uniform, finely divided crystals. The $CaCO_3$ precipitate started while agglomerating Ca^{2+} and CO_3^{2+} cluster, and colloidal nuclei grow and become a stable crystal.

Inorganic mineral deposits, especially, calcium carbonate, were found in an aragonite form in nature. At ambient conditions, it forms stable calcite form while aragonite is the high-temperature polymorph. Vaterite is another thermodynamically unstable form [1]. Their transformation into stable calcite is usually problematic in oil and gas processes, paper production, thermal power plants, nuclear power stations, and desalination facilities [2].

The cost for maintenance and cleaning of scale pipelines and heat exchangers in industries is very high each year [3].

Calcium carbonate scaling is a dominant fouling mechanism bedeviling fluid-based sectors [4]. The deposit of carbonate minerals is a subject of vital interest due to its side effects in industrial processing, which has been continuing to challenge in ensuring flow assurance and continuous operation [5]. Much research has been done to evaluate a suitable scale inhibition technique that may mitigate the damage caused by scales in the oil and gas industry [6–8], among which are chemical and nonchemical based methods. It is worth mentioning that little work is reported on the role of light places in the fouling mechanism.

Calcium scale prevention involving chemicals is a common practice industry used for scale prevention in industrial fluid flow treatment. Chemical inhibitors are abundantly used in the industry. Functional groups like polyphosphate, phosphate esters, organic phosphonates, polyacrylates, and other various copolymers of phosphonates, carboxylate, and sulfonate help the inhibition of calcium carbonate [9, 10]. The following vital parameters were considered when selecting a suitable chemical inhibitor: solution composition, compatibility, stability, solubility, toxicity, hydrolytic stability, degradation level, and minimum inhibitory concentration (MIC) [11–13]. Temperature is another important factor considered in the choice of efficient chemical inhibitor. The MIC represents the minimum effective concentration of chemical scale inhibitors to prevent scaling in industrial processes [13, 14]. Recent findings have shown that the chemicals, as mentioned above, pose a great concern to the environment and public health and are also very expensive [15–17].

There are also some nonchemical based scale inhibitors that serve as an alternative to magnetic, electronic, and electrolytic processes [18–20]. Magnesium was another method employed in an attempt to mitigate the problems caused by scale formation in water treatment without the use of chemicals [21]. Even though earlier works done in this area were not entirely sure about the mechanism of the magnetic field in addressing this issue, [22] provided some insight into the research field. However, [21, 23] in their work suggested that the magnetic field modifies the nucleation stage and crystal growth, which goes a long way to affect the rate of formation and crystal deposition. Various experimental designs were proposed for electromagnetic antiscaling studies [2, 24, 25]. Among these studies, the heat exchanger with a magnetic field of an orthogonal flow fluid circulating the system maximizes the scale formation at a specific temperature and pH [26, 27].

It was observed that calcium carbonate was reduced by 50% after samples exposure to the magnetic field on the equilibrium of carbonates with the change in PH. The application of a magnetic field directly influences sample pH and the formation of crystal growth in the equilibrium condition. A reduction in the size of crystals was observed [22, 26, 27].

Applying the electric field is another nonchemical method reported in the literature to regulate the crystal growth rate of calcium carbonate [28]. Various strategies are reported on the electrical effectiveness potential on the antiscaling treatment of water, where [28, 29] focused on the way of preventing the scaling in water treatment. They used a pulsed spark discharge approach to enhance the precipitation of dissolved calcium ions in cooling towers. This process led to heat reduction in water hardness close to 20–26% and led to the conclusion that electrolysis was the reason for this observation. Applying high electric potential also helps to enhance bicarbonate dissociation [30]. Dhanasekaran and Ramasamy [31], in their work, asserted that the tendency for nucleation to occur is reduced with an increase in the strength of the electric field at certain angles.

According to [3, 24, 32], the effect of the electric field on calcium carbonate scale formation has been studied by applying an electric field on two graphite electrodes immersed in the working solution at different levels of voltage, frequency, and degree of supersaturation.

Little is known about the efficacy of ultraviolet light on calcium scale, and this particular work is to shed light on this area. Among the earlier mentioned methods, ultrasonic is tested to be more effective in the crystallization process [33–40]. The effect of applied ultrasonic on a liquid medium is that it exerts alternating and rarefaction within the liquid, generating bubbles at rarefaction stage. The bubbles outlive repeated cycles of compression and rarefaction until a critical size is reached, and breakdown occurs, starting what is known as cavitation. That is, the rapid formation, growth, and violent disruption of bubbles and chemical and physical changes are promoted due to powerful ultrasound. The mechanism of single or multibubble cavitation indicates that the collapsing bubble behaves as a particular microreactor where ions and radicals in the excited state are involved in the reaction outcome. Near the liquid-solid interface, cavity collapse leads to boundary layer destruction and mass/heat transfer improvements. The ultrasonic technique is seen as an effective way of achieving faster, proper, and uniform nucleation, comparatively easy nucleation of particles at lower supersaturation levels, and reduced agglomeration [41, 42].

However, deliberate efforts are geared toward developing more fouling retarding techniques that are low cost and remarkably benign to the environment. The finding shows that Dallas [31] has studied the effect of UV light on calcium carbonate scale formation, reporting inhibition of calcium carbonate scale compared to the untreated water.

2. Materials and Methods

2.1. Materials. Sigma-Aldrich, Germany, supplied calcium chloride ($CaCl_2.6H_2O$), sodium chloride (NaCl), sodium bicarbonate ($NaHCO_3$), and ethylenediaminetetraacetic acid (EDTA) of analytical grade. Hydrex 4102 RO antiscalant and polypropylene and polysulfone membranes are supplied by VEOLIA WATER STI, Khobar, Saudi Arabia. Hydrex 4102 chemical constituents are amino tris(methylene phosphonic acid) and phosphonic acid with a pH of 11.00–12.00 and a specific gravity of 1.35–1.45.

2.2. Methods. Synthetic seawater solution was prepared by mixing 86.0 mM sodium chloride, 4.50 mM calcium chloride, and 9.50 mM sodium bicarbonate solutions prepared

from standardized stock solutions prepared using deionized water using a Millipore Q-Plus 185 system. The pH of the solutions was measured by a glass/saturated calomel electrode (Metrohm), calibrated before and after each experiment with 4, 7, and 10 standard buffer solutions. The pH of the working solution was adjusted by the addition of hydrochloric acid and ammonia buffer. Calcium carbonate precipitation started when calcium chloride and sodium bicarbonate were added.

UV light was generated by a UV lamp source having a 15 mm diameter, $106\,\mu W/cm^2$ intensity, 54 V operating voltage, and 12 W output power, emitting broadband of UV light, with eight filters for specific wavelength selection, producing an average intensity of $2\,mW/cm^2$ at a distance of 2 cm from the working solution. Figure 1 shows the experimental setup of the UV treatment experiment. For the determination of the calcium ion concentration, 10 mL of the working solution was taken every 15 min, filtered by $0.025\,\mu m$ membrane filter, and titrated with EDTA standardized solution.

At the end of the experiments, the solutions were filtered, and the precipitates were collected and examined by XRD for the determination of crystal types of the deposited $CaCO_3$ scales. Sample sizes of 10×10 mm were prepared by manual cutting using a saw blade for each fouled tube and were analyzed at diffraction angles of 10 to 110°.

For the calcium carbonate scale deposition on membranes study, hydrophobic porous membrane (polypropylene) and hydrophilic membrane (polysulfone) were placed in the sample solution. The number of crystal deposits on the membrane was monitored at different intervals of time.

3. Results and Discussions

Calcium carbonate scale mitigation in water using UV light was only reported by [31]. Calcium carbonate is a sparingly soluble salt, growing by a parabolic rate law. Hence, the rate-limiting step of its crystal growth involves the dehydration of the growth units and the surface diffusion of these dehydrated growth units into the lattice from the adsorption site [31]. Calcium carbonate scale inhibition (CCI %) can be calculated by

$$CCI\% = \frac{[Ca^{2+}]_{sample} - [Ca^{2+}]_{blank}}{[Ca^{2+}]_{initial} - [Ca^{2+}]_{blank}} \times 100\%, \qquad (3)$$

where $[Ca^{2+}]_{blank}$ is the calcium ion concentration of the blank solution, $[Ca^{2+}]_{initial}$ is the calcium ion concentration at $t = 0$, and $[Ca^{2+}]_{sample}$ is the calcium ion concentration at time (t), respectively. The effect of antiscalants on calcium carbonate scale formation has been investigated by using ATMP (amino tris(methylene phosphonic acid)) as a scale inhibitor. ATMP, commercially named as Hydrex 4102, is one of the commonly used antiscalants used for calcium carbonate scale inhibition in water since it has an excellent chelating ability with calcium ions, low threshold inhibitory dosage, and powerful lattice distortion process. In chemical treatment experiments, different dosages of ATMP have
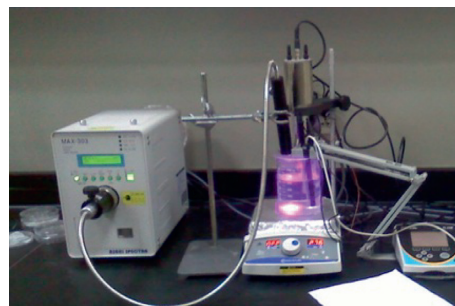

Figure 1: Experimental setup of UV treatment experiment.

been used, ranging from 1 to 10 mg/L, to test for the threshold concentration suitable for calcium carbonate scale inhibition.

Starting with 1 mg/L, CCI has increased by about 1% compared to the untreated system, as shown in Figure 1. When the dosage is 2 and 3 mg/L, the scale inhibition has increased by about 4%. Meanwhile, adding 5 mg/L has increased CCI to about 80% compared to 65% obtained for the control experiment. The 10 mg/L dosage achieved the best performance regarding scale inhibition, increasing CCI% to about 82% after 60 minutes. This finding indicates that 10 mg/L is the threshold inhibitory dosage of ATMP as calcium, a scale inhibitor for calcium carbonate (Figure 2).

The effect of the addition of ATMP during UV (265 nm) irradiation of the working solution has been investigated by adding antiscalant at different dosages from 1 to 10 mg/L. The addition of 1 and 2 mg/L increased the precipitation of calcium carbonate (Figure 3). Applying UV radiation dissociates the antiscalant into fragments that were unable to inhibit the scale formation. When increasing the dosage to 3 mg/L, the scale inhibition has been enhanced because the antiscalant molecules have blocked some of the active sites that are available for crystal growth. Meanwhile, increasing the antiscalant concentration to 5 mg/L and 10 mg/L has raised the scale inhibition to 96% compared to 36% for the untreated case.

3.1. Factors Affecting Scale Inhibition

3.1.1. Effect of pH. Figure 4 depicts the effect of pH on calcium carbonate scale inhibition using UV light of 265 nm radiation for 60 minutes. At a pH of 7.0, the scale inhibition was almost steady, reaching 97.1% after 60 minutes, while decreasing to 91.8% at a pH of 8. On the other hand, increasing pH to 9 had a drastic effect on the scale inhibition behavior, falling slowly in the first 15 minutes and then sharply decreasing in the next 15 minutes. After 60 minutes of exposure, the scale growth rate drops to 71% when compared to control samples.

This dramatic effect of pH can be interpreted based on the pH dependence of carbonate concentration in solution. Bicarbonate ions were dissociated into carbonate according to the following equation:
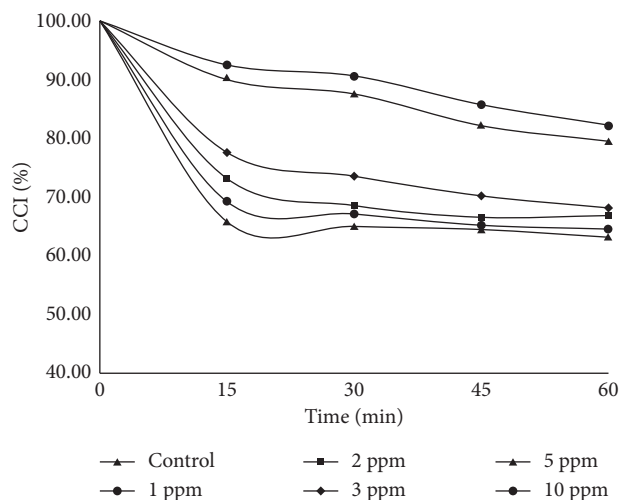
FIGURE 2: Effect of ATMP concentration on calcium carbonate scale formation changes the legend for 1 mg/L and 10 mg/L, as a function of time.
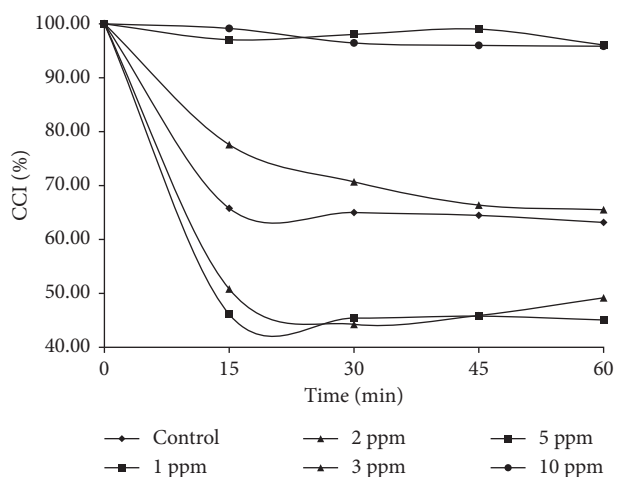

FIGURE 3: Influence of UV radiation on the ATMP concentrations on calcium carbonate scale inhibition, as a function of time.

$$HCO_3^- \rightleftharpoons CO_3^{2-} + H^+ \left(pK_a = 10.33\right) \qquad (4)$$

According to the Henderson-Hasselbalch equation, as pH increases, the carbonate concentration increases as indicated in Table 1:

$$pH = pK_a + \log \frac{[CO_3^{2-}]}{HCO_3^-} \qquad (5)$$

By increasing sample pH, an increase in the carbonate concentration by two orders of magnitude was noticed. An increase in sample pH also changes carbonate ions recombination, hence increasing the rate of calcium carbonate precipitation.

3.1.2. Effect of Radiation Energy.
The impact of radiation energy was studied in UV and visible regions. For the visible region, the solution was irradiated with 385 nm radiation,
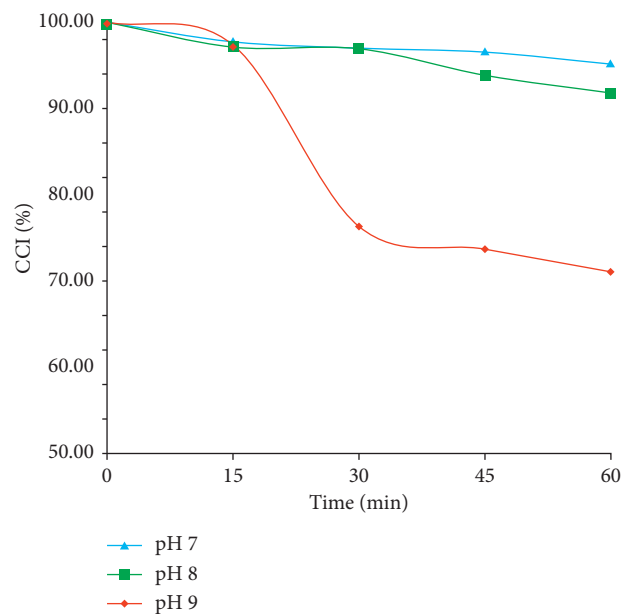

FIGURE 4: Effect of pH on calcium carbonate scale inhibition, as a function of time.

TABLE 1: Effect of pH on carbonate concentration in 9.50 mM bicarbonate solution.

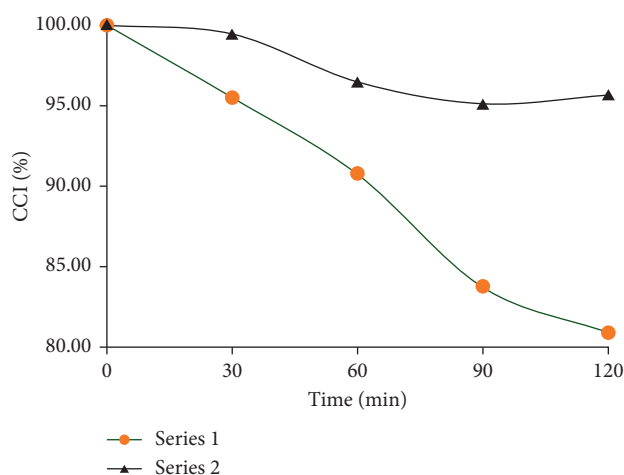| pH	$[CO_3^{2-}]$ (mM)
7	4.44×10^{-9}
8	4.44×10^{-8}
9	4.44×10^{-7}

FIGURE 5: Effect of radiation energy on calcium carbonate scale inhibition, as a function of time.

providing scale inhibition of 80.9% after 120 minutes, compared to 95.6% when irradiated with 265 nm UV radiation, as shown in Figure 5.

The effect of UV radiation can be explained through the calcium ion acid-base character. The calcium ion is a weak acid, and when excited, it becomes much more vulnerable.

TABLE 2: Rate of calcium carbonate crystal growth for UV-treated and UV-untreated water.

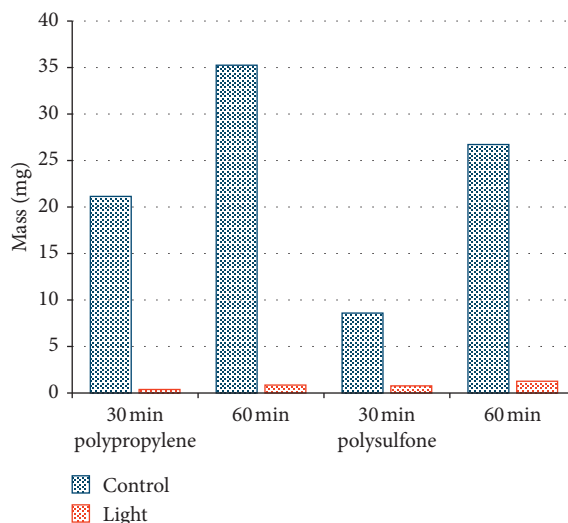| Water sample	$f(s)$	R ($\times 10^{-8}$ mol^{-2}s^{-1})
Untreated	1.05	7.36
Hydrex 4102	0.92	4.22
385 nm	0.92	1.87
265 nm	0.68	1.12

FIGURE 6: Weight measurements of calcium carbonate deposits with and without UV light treatment.
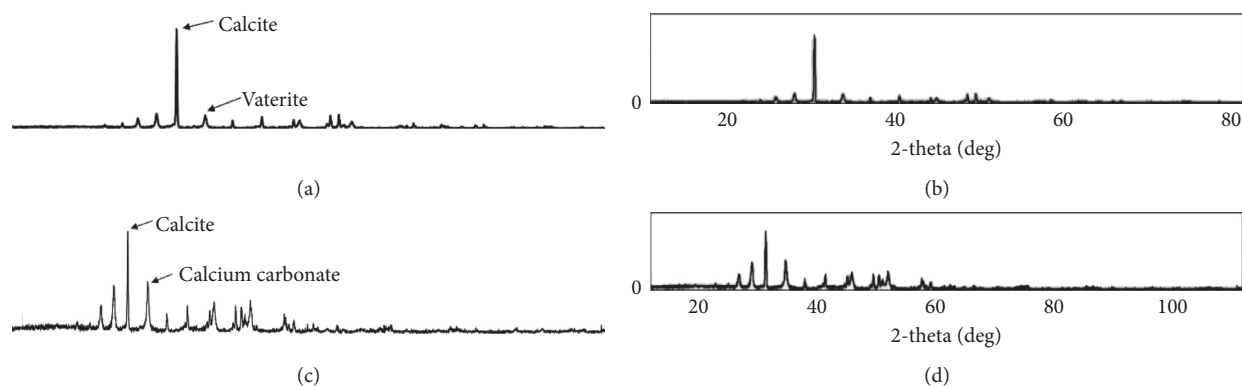

(a)

(b)

(c)

(d)

FIGURE 7: XRD spectra for (a) untreated case and (b) standard peaks of calcite and Vaterite and for (c) UV-treated case and (d) standard peaks of calcite and calcium carbonate.

Applying 385 nm visible light excites some of the energetic calcium ions becoming weakly acidic, and these acidic ions prevent recombination. When shifting from visible to UV region, the radiation energy increases, exciting more calcium ions, resulting in much more efficient scale inhibition.

3.2. Calcium Carbonate Crystal Growth Rate.

Calcium carbonate scale formation involves supersaturation, nucleation, crystal growth, and precipitation. Thus, affecting any of these steps can retard the crystal growth rate. Table 2 shows the percentage of crystal growth of calcium carbonate for the untreated, chemically treated, and irradiated water samples. The rate of crystal growth decreased by about 43% when

adding 3 mg/L of Hydrex 4102 antiscalant. The chemical antiscalant might be blocking some of the active sites of the calcium carbonate nuclei, therefore, decreasing the number of calcium carbonate crystals precipitated. The effect of UV radiation can be explained through the calcium ion acid-base character. When the calcium ions are subjected to UV radiation, some of the excited, energetic calcium ions become weakly acidic, and it reduces the recombination of calcium carbonate crystal growth. The crystal growth rate decreased by about 75% when water was irradiated with 385 nm. When shifting from visible to UV region, 265 nm, the radiation energy increases, exciting more calcium ions, degrading the crystal growth by about 85%. Thus, 265 nm UV radiation was used for further studies. Hence, UV light
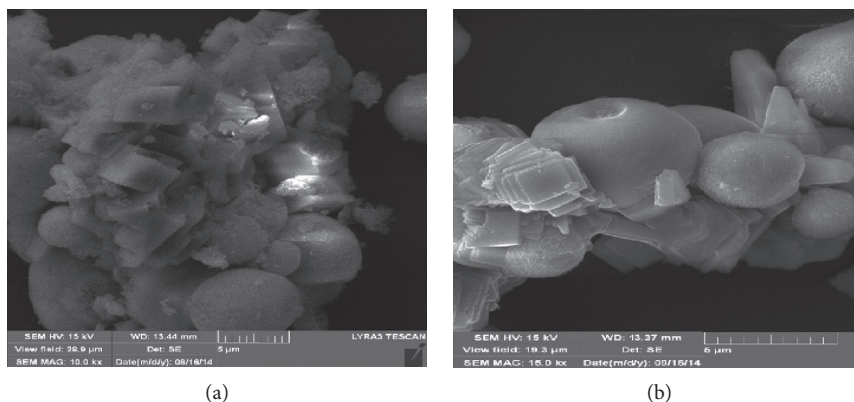
(a)

(b)

FIGURE 8: SEM images for deposits of (a) untreated water and (b) UV-treated water.

treatment is much more efficient in calcium carbonate scale inhibition compared to commercial antiscalants. The application of UV light has more advantages than chemical treatment. The UV radiation is commonly used in water treatment to get rid of pathogens without having any harmful effect when compared to chemical antiscalants.

The rate of crystal growth depends on the relative supersaturation and the number of the available surface active sites according to the following equation:

$$R = k_g \cdot f(s) \cdot \sigma^n, \tag{6}$$

where k_g is the crystal growth rate constant, $f(s)$ is a function of the number of available active sites for crystal growth, σ is the relative supersaturation, and n is the order of crystal growth, respectively.

3.3. Characterization of Scale Deposits

3.3.1. Membrane Scale Deposit Measurements. The amount of calcium carbonate deposited on polypropylene and polysulfone membranes was investigated by immersing the membrane separately inside the working solutions from 30 to 60 minutes. The amount of scale deposited for UV-treated samples is very low compared to the untreated one (Figure 6). This observation is precious for predicting the lifetime of the desalination membranes that are affected by the amount of scale deposited. Thus, using a UV light for scale inhibition increases the lifetime of the membrane due to the reduced membrane fouling.

3.3.2. XRD Analysis. Figure 7 shows XRD images of the deposits obtained from untreated and UV light treated water. The untreated control sample produces calcite and vaterite form of crystals. Interestingly, only calcite was formed in the case of the UV light treated samples. These crystals are less dense, less adherent, and easily removable when deposited compared to aragonite [11].

3.3.3. SEM Analysis. SEM images of the deposits obtained from untreated and UV light treated water are shown in Figure 8. The SEM images reveal that calcite crystals with small particle sizes for the UV radiation samples and vaterite form control samples.

4. Conclusion

In the reported work, we investigated the scale inhibition property of ultraviolet light on calcium carbonate. An outcome is an excellent approach to the calcite scale problem that is bedeviling the oil and liquid-based industries over the years. The following are the conclusions drawn from this study.

(1) Applying UV light, the calcium carbonate crystal growth rate decreased by about 85% when compared to 43% for 3 mg/L spiked amino tris(methylene phosphonic acid) antiscalant.

(2) Experimental results on polypropylene and polysulfone membranes deposition study indicate that the amount of scale deposited in the case of a UV-treated sample is insignificant when compared to the untreated one. Hence, it is expected that UV treatment might increase the lifetime of the membrane.

(3) XRD and SEM analyses revealed that UV light treatment produced mostly calcite crystals, which are less dense, less adherent, and easily removable than other types of calcium carbonate phases, hence increasing the lifetime of the membrane.

(4) We believe that UV radiation is an efficient green approach for calcium carbonate scale mitigation on membrane surfaces.

Data Availability

The data used to support the findings of this study are included in the article.

Disclosure

The manuscript is part of the M.S. thesis "Calcium Carbonate Scale Inhibition by Non-Chemical Methods."

Conflicts of Interest

The authors declare that they have no conflicts of interest.

Acknowledgments

References

[1] C. Perdikouri, A. Kasioptas, C. V. Putnis, and A. Putnis, "The effect of fluid composition on the mechanism of the aragonite to calcite transition," *Mineralogical Magazine*, vol. 72, no. 1, pp. 111–114, 2008.

[2] A. Al Helal, A. Soames, R. Gubner, S. Iglauer, and A. Barifcani, "Influence of magnetic fields on calcium carbonate scaling in aqueous solutions at 150°C and 1 bar," *Journal of Colloid and Interface Science*, vol. 509, pp. 472–484, 2018.

[3] L. D. Tijing, D.-H. Lee, D.-W. Kim, Y. I. Cho, and C. S. Kim, "Effect of high-frequency electric fields on calcium carbonate scaling," *Desalination*, vol. 279, no. 1–3, pp. 47–53, 2011.

[4] D. J. Kukulka and M. Devgun, "Fluid temperature and velocity effect on fouling," *Applied Thermal Engineering*, vol. 27, no. 16, pp. 2732–2744, 2007.

[5] L. K. Abidoye and D. B. Das, "Scale dependent dynamic capillary pressure effect for two-phase flow in porous media," *Advances in Water Resources*, vol. 74, pp. 212–230, 2014.

[6] Z. Amjad, R. W. Zuhl, and S. Huang, "Deposit control polymers: types, characterization, and applications," in *The Science and Technology of Industrial Water Treatment*, Taylor & Francis Group, Abingdon, UK, 2010.

[7] L. A. Jackson, "Applications of cationic polymers in water treatment," in *The Science and Technology of Industrial Water Treatment*, Taylor & Francis Group, Abingdon, UK, 2010.

[8] V. Malkov and P. Kiser, "Recent Development in Water Treatment Chemicals Monitoring," in *The Science and Technology of Industrial Water Treatment*, Taylor & Francis Group, Abingdon, UK, 2010.

[9] N. Abdel-Aal and K. Sawada, "Inhibition of adhesion and precipitation of $CaCO_3$ by aminopolyphosphonate," *Journal of Crystal Growth*, vol. 256, no. 1-2, pp. 188–200, 2003.

[10] C. Wang, S.-p. Li, and T.-d. Li, "Calcium carbonate inhibition by a phosphonate-terminated poly(maleic-co-sulfonate) polymeric inhibitor," *Desalination*, vol. 249, no. 1, pp. 1–4, 2009.

[11] H. F. L. Santos, B. B. Castro, M. Bloch et al., "A physical model for scale growth during the dynamic tube blocking test," in *Proceedings of the OTC Brasil. Offshore Technology Conference*, Houston, TX, USA, May 2017.

[12] A. L. Graham, L. S. Boak, A. Neville, and K. S. Sorbie, "How minimum inhibitory concentration (MIC) and sub-MIC concentrations affect bulk precipitation and surface scaling rates," in *Proceedings of SPE International Symposium on Oilfield Chemistry*, Society of Petroleum Engineers, The Woodlands, TX, USA, 2005.

[13] Z. Amjad, *Mineral Scales in Biological and Industrial Systems*, CRC Press, Boca Raton, FL, USA, 2013.

[14] I. B. Silva, J. C. Queiroz Neto, and D. F. S. Petri, "The effect of magnetic field on ion hydration and sulfate scale formation," *Colloids and Surfaces A: Physicochemical and Engineering Aspects*, vol. 465, pp. 175–183, 2015.

[15] J. K. Daniels, I. Littlehales, L. Lau, and S. Linares-Samaniego, "Laboratory methods for scale inhibitor selection for HP/HT fields," in *Proceedings of the SPE International Oilfield Scale Conference and Exhibition*, Society of Petroleum Engineers, Aberdeen, Scotland, 2014.

[16] Aloe Derived Scale Inhibitor, 2009.

[17] J. K. Fink, "Scale inhibitors," *Petroleum Engineer's Guide to Oil Field Chemicals and Fluids*, pp. 253–274, 2012, https://www.academia.edu/39666846/Petroleum_Engineers_Guide_to_Oil_Field_Chemicals_and_Fluids_-_Johannes_Karl_Fink.

[18] N. Andritsos and A. J. Karabelas, "The influence of particulates on CaCO3 scale formation," *Journal of Heat Transfer*, vol. 121, no. 1, pp. 225–227, 1999.

[19] J. MacAdam and S. A. Parsons, "Calcium carbonate scale formation and control," *Reviews in Environmental Science and Bio/Technology*, vol. 3, no. 2, pp. 159–169, 2004.

[20] W. N. Al Nasser, A. H. Al Ruwaie, M. J. Hounslow, and A. D. Salman, "Influence of electronic antifouling on the agglomeration of calcium carbonate," *Powder Technology*, vol. 206, no. 1-2, pp. 201–207, 2011.

[21] A. Alabi, M. Chiesa, C. Garlic, and G. Palmisano, "Advances in anti-scale magnetic water treatment," *Environmental Science: Water Research and Technology*, vol. 1, no. 4, pp. 408–425, 2015.

[22] J. S. Baker and S. J. Judd, "Magnetic amelioration of scale formation," *Water Research*, vol. 30, no. 2, pp. 247–260, 1996.

[23] R. A. Barrett and S. A. Parsons, "The influence of magnetic fields on calcium carbonate precipitation," *Water Research*, vol. 32, no. 3, pp. 609–612, 1998.

[24] D. Hasson and D. Bramson, "Effectiveness of magnetic water treatment in suppressing calcium carbonate scale deposition," *Industrial & Engineering Chemistry Process Design and Development*, vol. 24, no. 3, pp. 588–592, 1985.

[25] D. Hasson, R. Semiat, D. Bramson, M. Busch, and B. Limoni-Relis, "Suppression of $CaCO_3$ scale deposition by antiscalants," *Desalination*, vol. 118, no. 1–3, pp. 285–296, 1998.

[26] J. Sohaili, H. S. Shi, Lavania-Baloo, N. H. Zardari, N. Ahmad, and S. K. Muniyandi, "Removal of scale deposition on pipe walls by using magnetic field treatment and the effects of magnetic strength," *Journal of Cleaner Production*, vol. 139, pp. 1393–1399, 2016.

[27] S. A. Parsons, B.-L. Wang, S. J. Judd, and T. Stephenson, "Magnetic treatment of calcium carbonate scale—effect of pH control," *Water Research*, vol. 31, no. 2, pp. 339–342, 1997.

[28] X.-k. Xing, C.-f. Ma, Y.-c. Chen, Z.-h. Wu, and X.-r. Wang, "Electromagnetic anti-fouling technology for prevention of scale," *Journal of Central South University of Technology*, vol. 13, no. 1, pp. 68–74, 2006.

[29] Y. Yang, H. Kim, A. Starikovskiy, A. Fridman, and Y. I. Cho, "Application of pulsed spark discharge for calcium carbonate precipitation in hard water," *Water Research*, vol. 44, no. 12, pp. 3659–3668, 2010.

[30] X. Xiaokai, "Research on the electromagnetic anti-fouling technology for heat transfer enhancement," *Applied Thermal Engineering*, vol. 28, no. 8-9, pp. 889–894, 2008.

[31] R. Dhanasekaran and P. Ramasamy, "Two-dimensional nucleation in the presence of an electric field," *Journal of Crystal Growth*, vol. 79, no. 1-3, pp. 993–996, 1986.

[32] M. Asraf-Snir, J. Gilron, and Y. Oren, "Gypsum scaling of anion exchange membranes in electrodialysis," *Journal of Membrane Science*, vol. 520, pp. 176–186, 2016.

[33] M. Su, J. Han, Y. Li, J. Chen, Y. Zhao, and K. Chadwick, "Ultrasonic crystallization of calcium carbonate in presence of seawater ions," *Desalination*, vol. 369, pp. 85–90, 2015.

[34] T. Waly, M. D. Kennedy, G.-J. Witkamp, G. Amy, and J. C. Schippers, "The role of inorganic ions in the calcium

carbonate scaling of seawater reverse osmosis systems," *Desalination*, vol. 284, pp. 279–287, 2012.

[35] B. E.-Y. Jibril and A. A. Ibrahim, "Chemical conversions of salt concentrates from desalination plants," *Desalination*, vol. 139, no. 1–3, pp. 287–295, 2001.

[36] W. N. Al Nasser, K. Pitt, M. J. Hounslow, and A. D. Salman, "Monitoring of aggregation and scaling of calcium carbonate in the presence of ultrasound irradiation using focused beam reflectance measurement," *Powder Technology*, vol. 238, pp. 151–160, 2013.

[37] L. Boels, R. M. Wagterveld, M. J. Mayer, and G. J. Witkamp, "Seeded calcite sonocrystallization," *Journal of Crystal Growth*, vol. 312, no. 7, pp. 961–966, 2010.

[38] Z. Guo, A. G. Jones, and N. Li, "The effect of ultrasound on the homogeneous nucleation of," *Chemical Engineering Science*, vol. 61, no. 5, pp. 1617–1626, 2006.

[39] I. Nishida, "Precipitation of calcium carbonate by ultrasonic irradiation," *Ultrasonics Sonochemistry*, vol. 11, no. 6, pp. 423–428, 2004.

[40] E. Dalas, "The effect of the ultrasonic field on calcium carbonate scale formation," *Journal of Crystal Growth*, vol. 222, no. 1-2, pp. 287–292, 2001.

[41] D. Chen, S. K. Sharma, and A. Mudhoo, *Handbook on Applications of Ultrasound : Sonochemistry for Sustainability*, CRC Press, Boca Raton, FL, USA, 2012.

[42] B. Pečnik, M. Hočevar, B. Širok, and B. Bizjan, "Scale deposit removal utilizing ultrasonic cavitation," *Wear*, vol. 356, pp. 45–52, 2016.

Research Article

Preparation of Highly Stable and Effective N-Doped TiO₂@SiO₂ Aerogel Catalyst for Degradation of Organic Pollutants by Visible Light Catalysis

Shiyun Tang [1,2] **Jingyu Ran,**[1,2] **Junjiang Guo,**[1,2] **and Anjiang Tang**[1,2]

^{1}*College of Chemical Engineering, Guizhou Institute of Technology, Guiyang 550003, China*
^{2}*Engineering Technology Research Center of Fluorine Silicon Material, Guiyang 550003, China*

Correspondence should be addressed to Shiyun Tang; 524506512@qq.com

To obtain high stable and effective TiO_2 photocatalyst, nano-N-doped $TiO_2@SiO_2$ ($TiO_{2-x}N_x@SiO_2$, $0 \leq x \leq 2$) composite aerogels were synthesized by the sol-gel method combined with supercritical drying and direct oxidation process. The adsorption/ photocatalytic degradation efficiency of $TiO_{2-x}N_x@SiO_2$ aerogels was evaluated by the degradation of RhB in aqueous solution under visible light irradiation. The physiochemical properties of the aerogels were examined by XRD, FT-IR, TEM, SEM, TG/ DTA, and BET methods. It was found that the specific surface areas of all $TiO_{2-x}N_x@SiO_2$ samples exceeded 700 m^2/g and exhibited a honeycomb porous structure with fine particulate morphology. Photocatalytic activity tests show that the 500-$TiO_2@$ SiO_2 composite aerogel exhibits the best adsorption/photocatalytic degradation rate for RhB, which obtained about 80% of the degradation rate in 30 min under visible light and over 95% after 120 min. On the one hand, the SiO_2 aerogels can significantly inhibit the phase transition of TiO_2, and the nano TiO_2 can be highly dispersed in the SiO_2 aerogels; On the other hand, if the oxidation temperature is selected properly, the N-doped $TiO_{2-x}N_x@SiO_2$ aerogel can be obtained by simple TiN@SiO_2 aerogel oxidation.

1. Introduction

Titanium oxide (TiO_2) is an excellent semiconductor photocatalyst because of its high photocatalytic activity, good chemical stability, safety, nontoxicity, and low cost without secondary pollution [1–3]. In the past decades, TiO_2 as photocatalytic materials has become the important subject of attention by many researchers at home and abroad, in the water/air treatment [4], solar cell electrodes [5], water decomposition for hydrogen production [6], and other fields. It has three polymorphs in nature: anatase, rutile, and brookite. The main photocatalytic activities are anatase and rutile TiO_2. Rarely researchers focus on brookite TiO_2 due to its little photocatalytic activity and low thermal stability [7]. However, owing to the rather high intrinsic bandgap of pure TiO_2 (about 3.0 eV), only 3%–5% of the incoming solar energy on the earth's surface can be utilized. Many problems

still restrict the practical application of TiO_2 as a photocatalyst with excellent performance, such as low quantum efficiency, narrow light absorption wavelength, low solar energy utilization, and poor adsorption and recycling in the suspended phase photocatalytic system of water treatment.

To improve the photocatalytic efficiency of TiO_2, an extensive interest is invested in the use of metal or nonmetal as dopant during the preparation process. This principle is based on the "band filling mechanism;" the bandgap energy can be increased by doping metallic ions or nonmetallic element because the photoexcited electrons can be confined in the conduction band; thus, their lifetime can be prolonged [8]. Although metal and nonmetallic ion modification methods can improve the performance of TiO_2 photocatalyst to some extent, TiO_2 doped with metal ions is often thermounstable and the carrier recombination rate increases, thus sacrificing its photocatalytic ability in the ultraviolet

(UV) region. On the contrary, TiO_2 doped with nonmetallic can not only enhance the visible light response ability but also maintain the photocatalytic activity in the UV region. Therefore, the nonmetallic ions doping in TiO_2 photocatalyst has shown great industrial application prospects. At present, the research studies on doping of nonmetallic ions are mainly focused on C [9], N [10], S [11], and F [12]. Among them, N is easy to be introduced into the structure of TiO_2 because of the comparable atomic radius to O atom, low ionization energy, and high stability. N-doped TiO_2 composite oxides always use the concentrated $NH_3 \cdot H_2O$ or NH_4F as nitrogen and fluorine source [13]. The photocatalytic activity of TiO_2 can be significantly improved with the addition of N [14, 15]. Therefore, N-doped TiO_2 has become the most promising doping method for nonmetallic doping.

Moreover, to obtain the high-performance photocatalyst, nanosized TiO_2 is often used due to the higher photocatalytic activity than ordinary TiO_2. Nevertheless, TiO_2 nanoparticles tend to aggregate, which reduce its efficiency. To solve this problem, this work employs the SiO_2 aerogel as a support for TiO_2 nanoparticles, which make TiO_2 nanoparticles highly dispersed in SiO_2 aerogels, thus preventing its aggregation. SiO_2 aerogel is a solid material composed of nanoparticles or polymer molecules, which are crosslinked to form nanoporous skeleton structure. The unique nanoscale skeleton and pore distribution feature endow its excellent performance, such as ultralow density (as low as $0.003 \, g/cm^3$), high porosity (above 90%), huge specific surface area ($500–1200 \, m^2/g$), strong transmittance (about 93%), low refractive index, and small dielectric constant (<1.01) [16–18]. Owing to these characteristics, SiO_2 aerogel has a broad application prospect in the field of thermal insulation materials, sound insulation materials, filter materials, catalysts, adsorbents, sensors, fuel cells, etc. [19–21].

It is important to combine the excellent properties of aerogels with nanophotocatalysts to take full advantage of the high adsorption efficiency and strong transmittance of SiO_2 aerogel and photocatalytic activity of nanosized TiO_2 photocatalyst simultaneously. The nano-$TiN@SiO_2$ composite aerogel materials were prepared by the sol-gel method combined with supercritical drying process. Then, the nano-N-doped $TiO_2@SiO_2$ ($TiO_{2-x}N_x@SiO_2$, $0 \leq x \leq 2$) composite aerogels were obtained by the direct oxidation method. Finally, the adsorption/photocatalytic degradation efficiency for Rhodamine B (RhB) in aqueous solution of the $TiO_{2-x}N_x@SiO_2$ composite aerogels have been analyzed and discussed. This preparation process of aerogels can be either supercritical drying or ambient pressure drying [22, 23], and it can be easily scaled up for industrial production of visible light-driven N-doped TiO_2 photocatalyst for pollutants removal because of its convenience and energy-saving properties.

2. Experimental Details

2.1. Materials. Nano-TiN powder (≥99.9%) with a particle size of 20 nm and density of $5.24 \, g/cm^3$ was purchased from Shanghai Aladdin Biochemical Technology Co., Ltd.

Tetraethoxysilane (TEOS), absolute ethanol (C_2H_5OH), hydrochloric acid (HCl), ammonia ($NH_3 \cdot H_2O$), and RhB were obtained from ScienceLab Instrument Inc., Guizhou. All the reagents were of analytical grade purity and used without further purification. Deionized water was used throughout the experiment.

2.2. Preparation of $TiO_{2-x}N_x@SiO_2$ Composite Aerogel. Nano-$TiN@SiO_2$ composite aerogel was synthesized through the sol-gel method with the high-temperature supercritical drying. The procedure is as follows: Firstly, a certain amount of C_2H_5OH and TEOS were put into water (The volume ratio of $C_2H_5OH : TEOS : H_2O$ is $1 : 3 : 6$) and dispersed by ultrasonic oscillation for 30 min at room temperature. Then, adding 1 mol/L HCl as catalyst, adjusting pH value to 1.5–2.5 under magnetic stirring for 2 hours, followed by addition of 0.2 mol/L $NH_3 \cdot H_2O$ slowly until the pH value is 7-8. At the same time, appropriate amount of nano-TiN powder (the theoretical wt.% of TiN is 10%) was added rapidly under intense stirring. The solution was continuously stirred for 2.5 h and subsequently aged for 2 h to obtain $TiN@SiO_2$ gel with appropriate viscosity. Prior to supercritical drying, the gel was soaked in ethanol for 4-5 times, and the aging solution was replaced every 24 h. Finally, the gel was transferred to an autoclave with admitting nitrogen gas into the chamber at about 2 MPa. Heating was carried out at a rate of 1°C/min until 260°C. This was chosen as the supercritical temperature for the ethanol solvents and the necessity to avoid any thermal decomposition of the solvent. The pressure inside the autoclave gradually increases to about 8 MPa when the supercritical temperature was achieved. The final pressure and temperature were maintained for at least 15 min. After that, the solvent was rapidly removed by opening the outlet valve to vent, and the autoclave was then allowed to cool to room temperature and disassembled. A black-colored aerogel powder of $TiN@SiO_2$ was obtained at this stage. To gain the $TiO_{2-x}N_x@SiO_2$ composite aerogel, the $TiN@SiO_2$ was ground into a finer powder and calcinated at the fixed temperature for 2 h in a furnace under air atmosphere. The samples were coded as calcinated temperature- $TiO_2@SiO_2$, e.g., the $TiN@SiO_2$ aerogels calcined at 300°C were recorded as 300-$TiO_2@SiO_2$. Color changed from black to light yellow N-doped $TiO_2@SiO_2$ ($TiO_{2-x}N_x@SiO_2$, $0 \leq x \leq 2$) composite aerogels after different temperature calcined.

2.3. Photocatalytic Activity Evaluation. The photocatalytic activity of $TiO_{2-x}N_x@SiO_2$ composite aerogel was evaluated by the degradation of RhB in aqueous solution under simulated solar irradiation with a 500 W Xenon lamp (Beijing Perfectlight Technology Co. LTD., PLS-SXE300/300 UV). The lamp was positioned inside a cylindrical vessel and surrounded by a circulating water jacket to cool it. An amount of 10 mg photocatalyst was totally suspended in a 100 ml aqueous solution of $10 \, mg \cdot L^{-1}$ RhB. The solution was treated by ultrasonic oscillation for 15 min at room temperature. Then, the solution was shined with visible light by removing ultraviolet light using a filter. The distance

between light source and the bottom of the solution was about 15 cm. At each time interval, 4 ml of the suspension was extracted for analysis during each photocatalytic process. Finally, the concentration of RhB was monitored by colorimetry with a UV-Vis spectrophotometer (Lambda35, PerkinElmer) at its maximum absorption wavelength. The adsorption/photocatalytic degradation efficiency of RhB was defined according to the following equation:

$$\eta\,(\%) = \frac{(C_0 - C_t)}{C_0} * 100\%, \tag{1}$$

where η is the adsorption/photocatalytic degradation rate, C_0 was the initial concentration of RhB, and C_t was the corresponding concentration of RhB at certain reaction time.

2.4. Characterization.

The specific surface area and pore size distribution of aerogels were determined by the Brunauer–Emmitt–Teller N_2 adsorption-desorption method (BET, HYA2010-B1). Pore size distribution and specific desorption pore volumes were obtained using the Barrett-Joyner-Halenda (BJH) method using the desorption branches. The surface morphology and porous structure of aerogel photocatalysts were observed by scanning electron microscopy (SEM, Nova Nano 450, FEI, USA) and transmission electron microscopy (TEM, Tecnai G^2 F20 S-TWIN, FEI, USA). The phase compositions of the samples were determined by X-ray diffraction analysis (XRD, Ultima IV, Rigaku Corporation, Japan), which was carried out in a DX-2500 rotating anode X-ray diffractometer using Cu $K\alpha$ ($\lambda = 0.15406$ nm) radiation within the 2θ range of 10–$80°$. Thermogravimetric and differential thermal analysis (TG/DTA, Beijing Everlasting Scientific Instrument Factory, ZH-1450) were performed in air atmosphere at a heating rate of $10°$C/min from the room temperature to $750°$C. Fourier transform infrared (FT-IR) spectra were recorded on a Spectrum VERTEX 80 spectrometer in the range of 400–$4000\,\mathrm{cm}^{-1}$.

3. Results and Discussion

3.1. Morphology and Structures of Composite Aerogels.

The N_2-BET is used to characterize the porosity and surface area of the as-prepared TiN@SiO$_2$ and TiO$_{2-x}$N$_x$@SiO$_2$ composite aerogels. A typical nitrogen adsorption-desorption isotherm and pore size distribution of TiN@SiO$_2$ composite aerogel is presented in Figure 1. According to IUPAC classification, the adsorption isotherm of TiN@SiO$_2$ aerogel corresponds to type-IV, which is considered to be due to the presence of mesopores in aerogel. The pore shape can be identified by the hysteresis loop, the TiN@SiO$_2$ aerogel shows the type-H2 hysteresis loop in relative pressure (P/P_0) ranges from 0.70 to 0.98, which suggests that the pore structures are complex and tend to be made up of interconnected networks with different sizes and shapes. Furthermore, the illustration of Figure 1 shows the pore size distributions measured by the BJH model. It is evident that there is a bimodal distribution, which was concentrated at 9.90 nm and 13.21 nm, respectively.
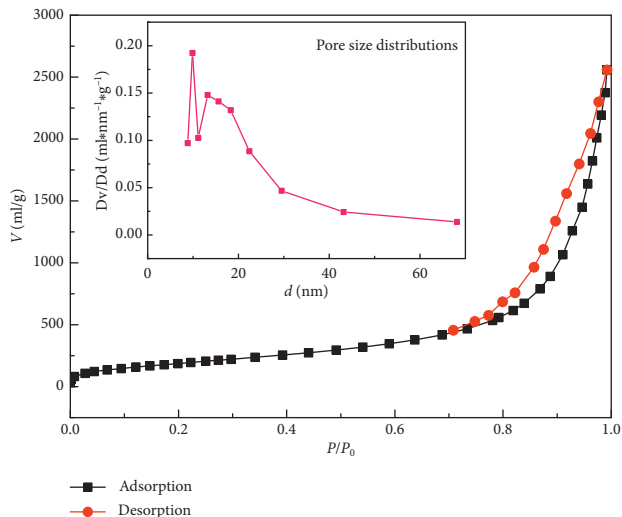

Figure 1: Adsorption-desorption isotherm and pore size distribution of TiN@SiO$_2$ composite aerogel.

Table 1: Specific surface area (S_{BET}), average diameter (d), and mesopore volume (V_p) of the aerogel samples.

Sample	S_{BET} (m^2/g)	d (nm)	V_p (cm^3/g)
As-prepared TiN@SiO$_2$	711	16.32	4.19
300-TiO$_2$@SiO$_2$	743	12.97	3.18
500-TiO$_2$@SiO$_2$	770	11.29	2.85
700-TiO$_2$@SiO$_2$	703	12.66	2.93

The specific surface areas of as-prepared TiN@SiO$_2$, 300-TiO$_2$@SiO$_2$, 500-TiO$_2$@SiO$_2$, and 700- TiO$_2$@SiO$_2$ composite aerogels are listed in Table 1. All samples were porous and developed a huge specific area (exceed $700\,\mathrm{m}^2$/g). Specifically, the specific surface of the as-prepared TiN@SiO$_2$ aerogel sample is $711\,\mathrm{m}^2$/g and slightly increases reaching about $743\,\mathrm{m}^2$/g after thermal oxidation at $300°$C for 2 h, then further increased to $770\,\mathrm{m}^2$/g after calcined at $500°$C for 2 h. However, the specific surface of 700-TiO$_2$@SiO$_2$ aerogel decreases to $703\,\mathrm{m}^2$/g as expected. It can be seen that the composite aerogels manage to preserve a substantial specific surface even with calcination at $700°$C. The average diameters of the pores obtained by BET analysis are 16.32 nm for as-prepared TiN@SiO$_2$, 12.97 nm for 300-TiO$_2$@SiO$_2$, 11.29 nm for 500-TiO$_2$@SiO$_2$, and 12.66 nm for 700-TiO$_2$@SiO$_2$, and the corresponding mesopore volumes are $4.19\,\mathrm{cm}^3$/g, $3.18\,\mathrm{cm}^3$/g, $2.85\,\mathrm{cm}^3$/g, and $2.93\,\mathrm{cm}^3$/g, respectively. It is obvious that the pore size of aerogels is relatively stable after calcination, which means that the aerogels have the high thermal stability.

SEM and TEM images are presented in Figure 2 for a few structural characteristic TiN@SiO$_2$ composite aerogel before and after thermal treatment. The SEM image of the as-prepared TiN@SiO$_2$ sample is shown in Figure 2(a). It can be seen that it exhibits a honeycomb porous structure with fine particulate morphology. The structure is quite uniform and amorphous flocculent on the whole. However, the accurate determination of crystallite size cannot be made by SEM. This was subsequently observed by using the TEM image
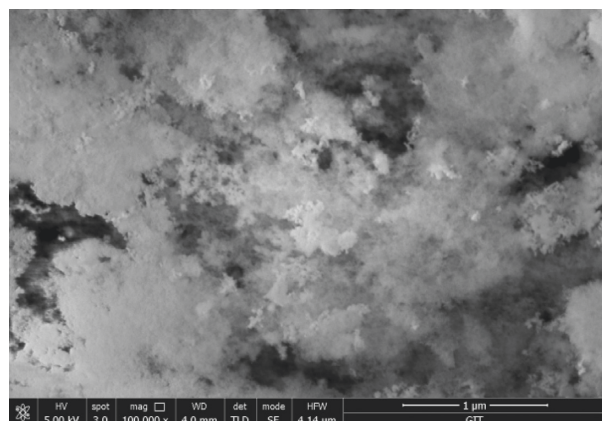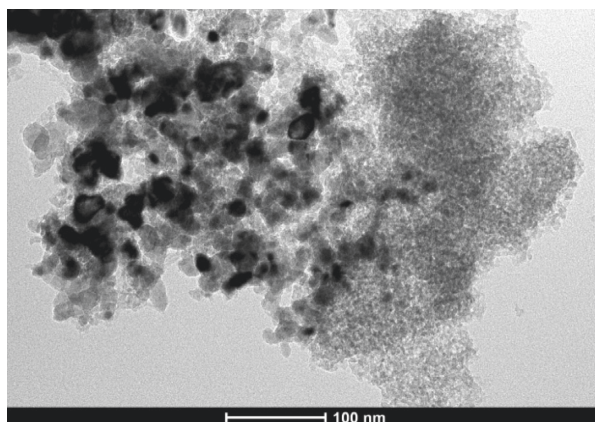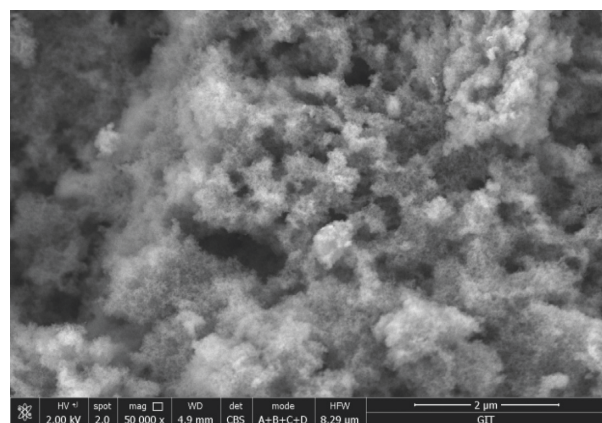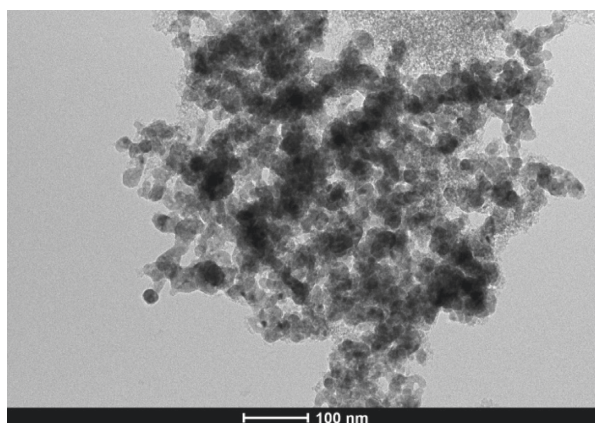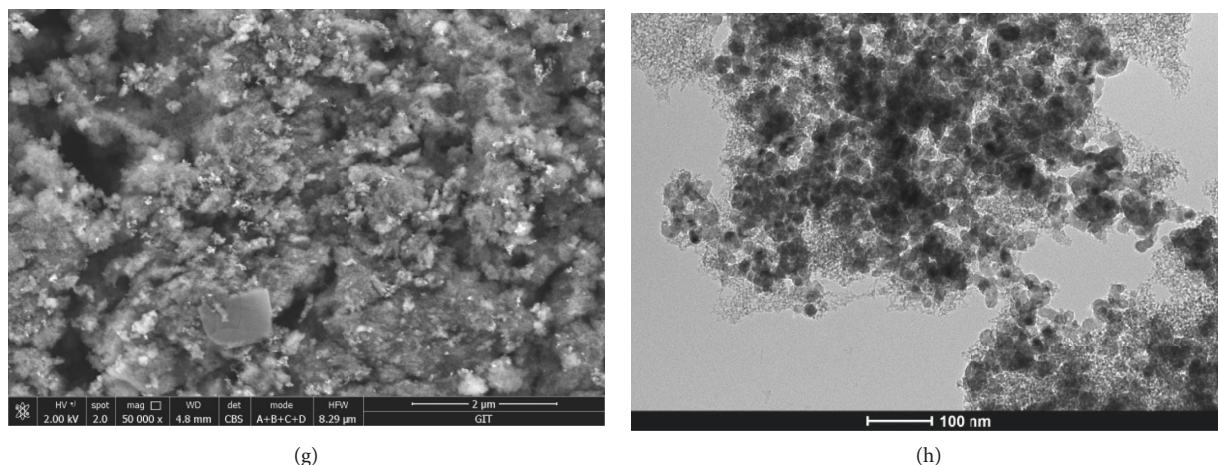
(a)
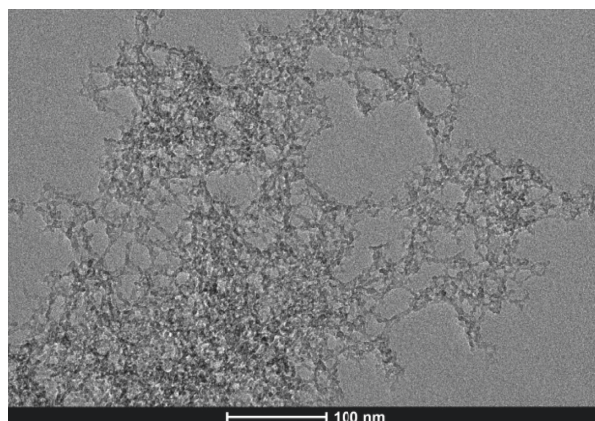
(b)
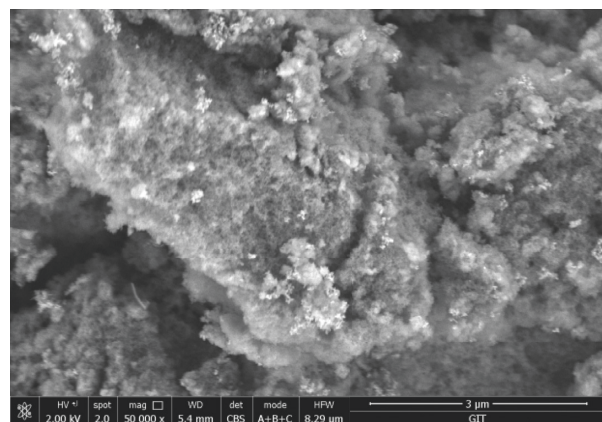
(c)

(d)

(e)

(f)

Figure 2: Continued.

(g)

(h)

FIGURE 2: SEM and TEM images of TiN@SiO$_2$ composite aerogels before and after thermal treatment: SEM (a) and TEM (b) of TiN@SiO$_2$; SEM (c) and TEM (d) of 300-TiO$_2$@SiO$_2$; SEM (e) and TEM (f) of 500-TiO$_2$@SiO$_2$; SEM (g) and TEM (h) of 700-TiO$_2$@SiO$_2$.

(Figure 2(b)), which revealed a porous nanostructure built up of small nanoparticles of size about 10 nm. After thermal oxidation at 300°C for 2 h, the bonding between particles is relatively close by SEM (Figure 2(c)), and the particles grow and sinter slightly at high temperature from TEM with higher magnification (Figure 2(d)). With the increase of oxidation temperature to 500°C, the microstructures of the samples hardly changed compared to 300-TiO$_2$@SiO$_2$ (see Figures 2(e) and 2(f)). However, when the oxidation temperature is further increased to 700°C, it can be observed that serious sintering phenomena with the number of large particles increase obviously (see Figures 2(g) and 2(h)). This trend is consistent with the previous BET results. When calcined at less than 500°C, the specific surface area of the material increases gradually due to the volatilization and pore expansion of residual ethanol in the aerogel. However, when the calcination temperature is up to 700°C, the specific surface area of the material begins to decrease due to the strong sintering effect.

3.2. Photocatalytic Activity of TiO$_{2-x}$N$_x$@SiO$_2$ Aerogels.

As is well known, RhB as an organic dye existed in water can cause serious water pollution problems [24]. In this work, the RhB was chosen as model molecules to investigate the adsorption/photocatalytic activity of TiO$_{2-x}$N$_x$@SiO$_2$ composite aerogels. The adsorption/photocatalytic degradation efficiency is a combination effect of adsorption and photodegradation. Figure 3 shows the adsorption/photocatalytic degradation efficiency (η) curves of TiO$_{2-x}$N$_x$@SiO$_2$ composite aerogels for RhB under visible light irradiation. It can be found that the η values for RhB increases with the extension of reaction time, and the 500-TiO$_2$@SiO$_2$ composite aerogel exhibits the best adsorption/photocatalytic degradation rate for RhB, which obtained about 80% of the degradation rate in 30 min under visible light and over 95% after 120 min. For the as-prepared TiN@SiO$_2$, the adsorption/photocatalytic degradation rate quickly reached about 60% in the first 30 minutes due to the strong adsorption capacity of aerogel, and it hardly
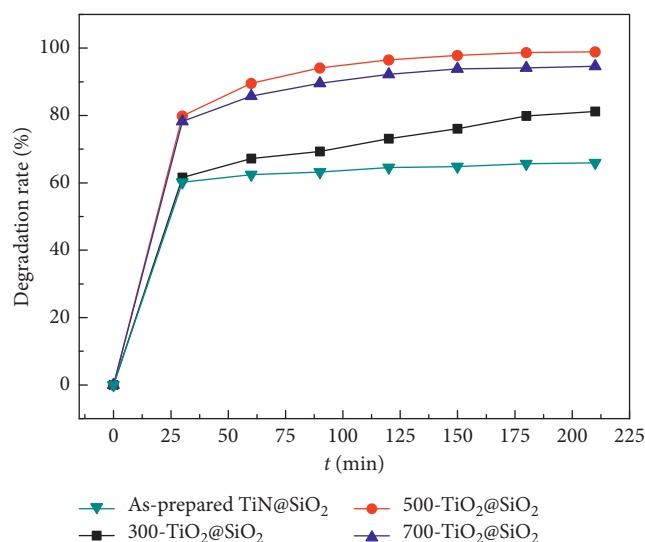

FIGURE 3: Adsorption/photocatalytic degradation rate curves of TiO$_{2-x}$N$_x$@SiO$_2$ composite aerogels for RhB under visible light irradiation.

increases with the increase of reaction time. According to previous BET analysis results, the mesoporous structure with higher pore volume of as-prepared TiN@SiO$_2$ composite aerogel is favorable for physical adsorption of RhB. Similar to as-prepared TiN@SiO$_2$, the adsorption/ photocatalytic degradation rate of the 300-TiO$_2$@SiO$_2$ also quickly reached about 62% in the first 30 minutes, but it increases slowly with the increase of reaction time. This indicates that the as-prepared TiN@SiO$_2$ composite aerogel has almost no visible-light photocatalytic activity, while the 300-TiO$_2$@SiO$_2$ has very weak visible photocatalytic activity. Furthermore, as the oxidation temperature increases, the adsorptivity capacity of 500-TiO$_2$@SiO$_2$ and 700-TiO$_2$@SiO$_2$ aerogels is significantly increased after heat treatment because of the improved hydrophilicity of TiN@SiO$_2$ composite aerogel in the heat treatment process.

3.3. Possible Photocatalytic Reaction Mechanism of $TiO_{2-x}N_x@SiO_2$ Aerogels.

To obtain the possible photocatalytic reaction mechanism of $TiO_{2-x}N_x@SiO_2$ aerogels, the phase composition, thermal stability, surface group, and absorbance properties as the increase of oxidation temperature were characterized by XRD, TG-DSC, FT-IR, and UV-Vis spectroscopy, respectively.

Figure 4 shows the XRD patterns of $TiN@SiO_2$ composite aerogels and TiN powers with different oxidation temperature. From Figure 4(a), it can be seen that all the samples have a dispersion characteristic peak at $15°–30°$, which indicates that these samples are mainly amorphous with a relatively low crystallinity. This is consistent with the results of SEM and TEM. For the as-prepared $TiN@SiO_2$ composite aerogel, the reflections at 2θ angles of $36.8°$, $42.7°$, and $62.0°$ belong to (111), (200), and (220) crystal face of NaCl-type structure of TiN (JCPDS card number 38-1420). As the oxidation temperature increases to $300°C$, there is no obvious change between the as-prepared $TiN@SiO_2$ and $300\text{-}TiO_2@SiO_2$ composite aerogel, and only the characteristic diffraction peaks corresponding to the (111), (200), and (220) crystal faces of TiN are presented. According to previous work [25], this can be explained that the oxidation of TiN at $300°C$ is very weak, and its significant initial oxidation temperature is about $350°C$. When the oxidation temperature is above $500°C$, the characteristic diffraction peaks of TiN are completely disappeared, and two very weak and dispersion diffraction peaks at $25.4°$ and $54.4°$ which belong to the (101) and (211) crystal faces of anatase-TiO_2 appear. Comparing $500\text{-}TiO_2@SiO_2$ with $700\text{-}TiO_2@SiO_2$ samples, it can be found that the intensity of (101) crystal plane of $700\text{-}TiO_2@SiO_2$ is slightly strong than that of $500\text{-}TiO_2@SiO_2$. This indicates that the $TiO_{2-x}N_x@SiO_2$ aerogels have an excellent thermal stability.

Figure 4(b) gives the XRD patterns of pure TiN powers after oxidation at $500°C$ and $700°C$. It can be seen that the pure TiN powers convert to anatase and rutile TiO_2 after oxidation at above $500°C$. The TiO_2 by calcined TiN powers has a series of obvious diffraction peaks with relatively narrow and acuity. Halo peaks or other signs of amorphous phases are not observed, which implies that the crystal phase structures of TiO_2 are relatively complete with a high crystallinity. It is noteworthy that the (101) and (200) reflections at 2θ angles of $25.4°$ and $48.2°$ of anatase-TiO_2 are more pronounced than (110) and (211) peaks at $27.5°$ and $54.4°$ of rutile TiO_2 for oxidation at $500°C$, respectively. But the case of the $700°C$ oxidation is just the opposite. This is due to the fact that other crystalline TiO_2 is easily transformed into more stable rutile structure at high temperatures [26]. The results are very different from $TiO_{2-x}N_x@SiO_2$ aerogels, because there are only weak and dispersed diffraction peaks of anatase TiO_2 observed in the latter. Considering the TiN wt.% of $TiN@SiO_2$ composite aerogels as 10%, the theoretical TiO_2 wt.% of $TiO_{2-x}N_x@SiO_2$ composite aerogels obtained by oxidation is 12.5%. The value is much higher than the detection limit of XRD. It means that the SiO_2 aerogels can significantly inhibit the phase transition of TiO_2 and the nano-TiO_2 can be highly dispersed in the SiO_2 aerogels.

From the XRD results, it seems that TiN in the $TiN@SiO_2$ composite aerogels can be completely oxidized to TiO_2 above $500°C$. However, it is well known that pure TiO_2 has good photocatalytic activity only under ultraviolet irradiation, which is inconsistent with our experimental results. To further illustrate the visible light photocatalytic activity and thermal stability of $TiO_{2-x}N_x@SiO_2$ aerogels, TG-DTA experiments were carried out with as-prepared SiO_2 aerogel and as-prepared $TiN@SiO_2$ composite aerogel, as shown in Figure 5. From Figure 5(a), pure SiO_2 aerogel has a small weight loss (about 5%) from room temperature to $215°C$ which is attributed to desorption of physical adsorption water. Then, a notable weight loss (about 15%) is observed from $215°C$ to $310°C$, which is attributed to the residual organic solvents in the aerogel. In the DTA curve, the decomposition of organic residues is reciprocated by the appearance of a remarkable endothermic peak with the maximum peak temperature (T_{max}) of $245°C$. Further weight loss (about 7.5%) is observed at a temperature range of $310–750°C$. This might be ascribed to the organic macromolecular formed by condensation of organic solvents during supercritical drying and further condensation of free $−OH$ groups on the SiO_2 network to form Si–O–Si bridges [27]. The TG curve of $TiN@SiO_2$ composite aerogel is similar to that of as-prepared SiO_2 on the whole (see Figure 5(b)). About 5% of weight loss belongs to the physical adsorption water at a temperature range of room temperature $−250°C$. A sharp weight loss (about 5%) of the residual organic solvents at a temperature range of $250–290°C$ is also observed, which shows a remarkable endothermic peak with T_{max} of $258°C$ in the corresponding DTA curve. However, there is obvious difference that the $TiN@SiO_2$ composite aerogel has a broad endothermic peak at a temperature range of $290–570°C$ with T_{max} of $512°C$ in the DTA curve, which should be attributed to the gradual oxidation of TiN in the SiO_2 aerogel. It indicates that the $TiN@SiO_2$ needs to be completely oxidized above $570°C$ to form the $TiO_2@SiO_2$. According to our previous works about the oxidation of TiN coatings [25], the oxidation of TiN coating can be divided into three stages: mild oxidation below $500°C$, moderate oxidation between 550 and $600°C$, and severe oxidation between 650 and $750°C$. Specifically, initial oxidation of TiN with a partial color change occurs at $350°C$ and remarkable oxidation of TiN occurs between 400 and $450°C$. Therefore, if the oxidation temperature is selected properly, the N-doped $TiO_{2-x}N_x@SiO_2$ aerogel can be obtained by simple $TiN@SiO_2$ aerogel oxidation.

Figures 6(a) and 6(b) present the FT-IR and UV-Vis spectra of $TiN@SiO_2$ composite aerogels with different oxidation temperature, respectively. From Figure 6(a), the bands at about $1640\,cm^{-1}$ and $3450\,cm^{-1}$ can be assigned to the bending and stretching vibrations of the O-H groups, respectively. This is mainly due to the hydrophilicity of aerogels prepared by supercritical drying, which makes it easy to absorb water and form surface hydroxyl groups. According to the results of Huang et al. [28], the hydroxyl groups and hydrogen bonds on the surface of aerogels could enhance its adsorption capacity for RhB; thus, it will facilitate the subsequent photocatalytic degradation. The peaks
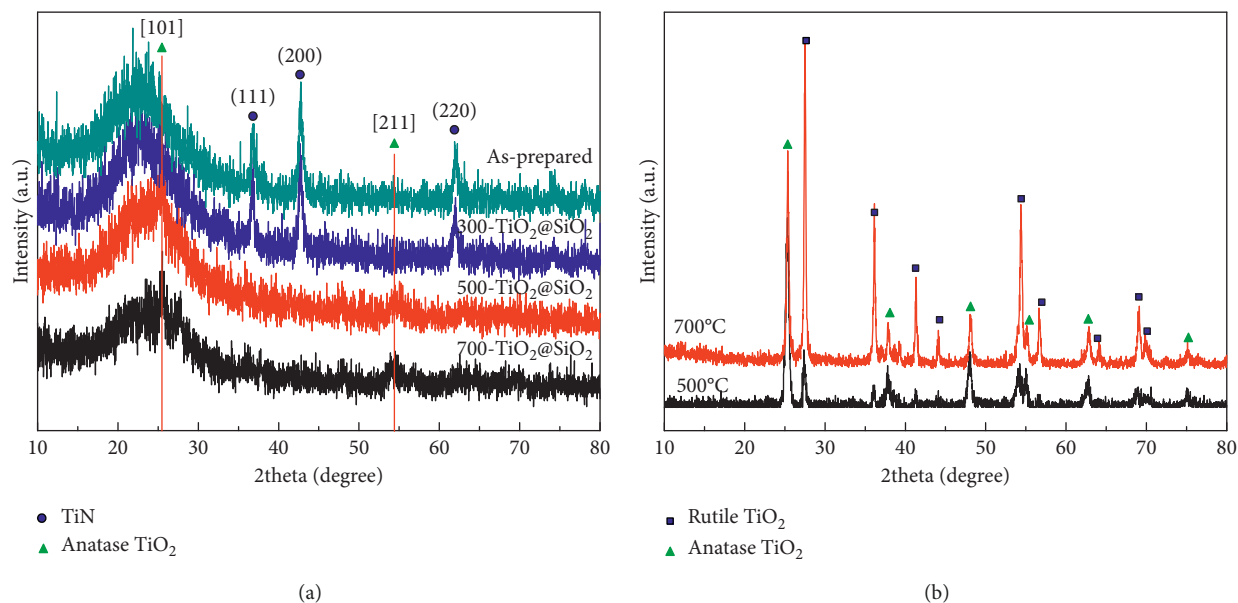
(a)

(b)

FIGURE 4: XRD patterns of TiN@SiO$_2$ composite aerogels (a) and TiN powers with different oxidation temperatures (b).
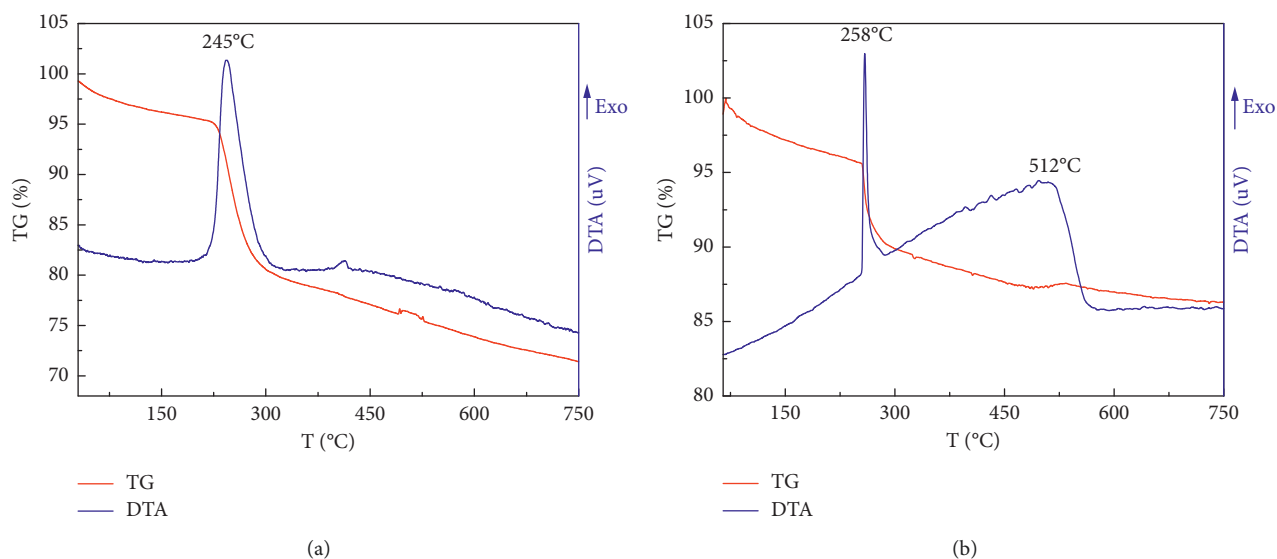

(a)

(b)

FIGURE 5: TG-DTA curves of SiO$_2$ aerogel (a) and TiN@SiO$_2$ composite aerogels (b).

assignable to symmetrical and asymmetrical stretching of Si-O-Si vibrations from the silica framework can be seen at 790–815 cm^{-1} and 1080–1100 cm^{-1}, respectively. It should be noted that there is the hetero-linkage Ti-O-Si bond at 940–960 cm^{-1} which indicates the incorporation of TiO$_2$ into SiO$_2$ to form binary TiO$_2$-SiO$_2$ systems. However, the expected Ti-N absorption bands (950–1000 cm^{-1}, 1100 cm^{-1} and 1300 cm^{-1}) [29] could not be observed because they were obscured by the strong absorptions bands in the region 950–1300 cm^{-1} from the silica framework. From Figure 6(b), the raw material SiO$_2$ aerogel exhibits almost no absorption from 300 to 800 nm. However, unlike pure TiO$_2$, which has no visible light absorption, the absorption of the TiN@SiO$_2$ composite aerogels becomes more obvious visible light absorption (>400 nm). And the increasing order of visible

light absorption intensity with different oxidation temperatures is 300-TiO$_2$@SiO$_2$, 700-TiO$_2$@SiO$_2$, 500-TiO$_2$@SiO$_2$.

Based on the above discussion and experimental results, it can be inferred that the possible reasons of highest efficiency of 500-TiO$_2$@SiO$_2$ composite aerogel are as follows: Firstly, it has the highest specific surface area of all samples. Secondly, N-doping can be formed by incomplete oxidation for the 500-TiO$_2$@SiO$_2$ composite aerogel, and the content of N-doped is moderate for photocatalysis. Moreover, the 500-TiO$_2$@SiO$_2$ composite aerogel exhibits the best visible light absorption after oxidation. It can also draw a schematic picture of the mechanism connected to the interaction of TiO$_{2-x}$N$_x$@SiO$_2$ aerogels under visible light, as shown in Figure 7. TiN@SiO$_2$ composite aerogel is oxidized to TiO$_{2-x}$N$_x$@SiO$_2$ aerogel at a certain temperature under air
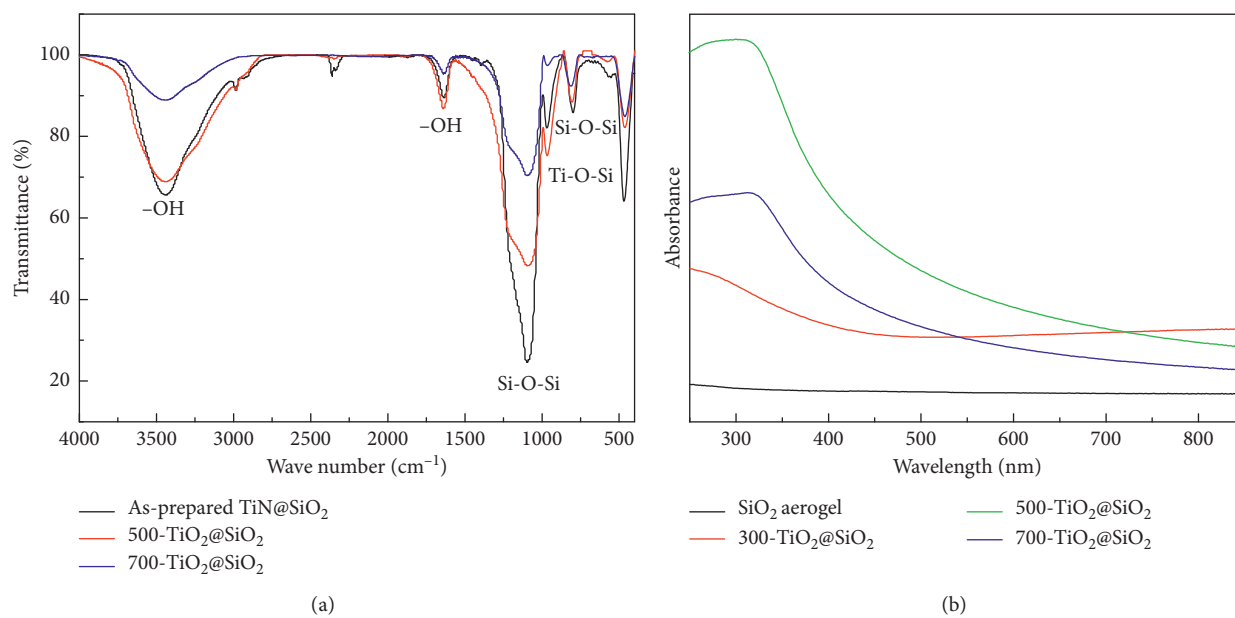
FIGURE 6: FT-IR (a) and UV-Vis (b) spectra of TiN@SiO$_2$ composite aerogels with different oxidation temperature.
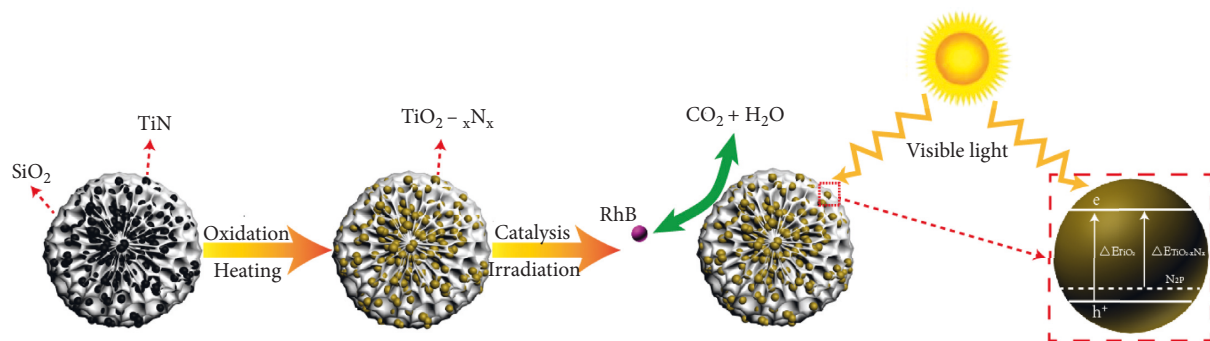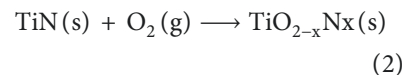

FIGURE 7: Sketch of the proposed mechanism for the processes induced by visible light irradiation of the TiO$_{2-x}$N$_x$@SiO$_2$ aerogels.

atmosphere; the reaction is shown in equation (1). Theoretically, if the oxidation temperature and time are chosen properly, the N-doped TiO$_2$@SiO$_2$ aerogels can be obtained due to the incomplete oxidation. Irradiation with visible light promotes the formation of the active oxygen species such as superoxide radicals and hydroxyl radicals [30, 31]. Numerous studies have shown that hydroxyl radicals are highly oxidative species which are considered to be the main species responsible for the photodegradation of the organic contaminants either adsorbed on the surface of the photocatalyst or in the bulk solution [32–34]. Therefore, the photocatalytic reaction can completely oxidize the RhB to form CO$_2$ and H$_2$O, as shown in equation (2). In fact, two effects must be considered with the final degradation efficiency when porous materials used as catalyst, the adsorption and degradation of the degradants. TiO$_2$ powers have a weak adsorption capacity, but SiO$_2$ aerogels can provide more adsorption centers; thus TiO$_2$@SiO$_2$ aerogels combine the advantage of high surface area and porous SiO$_2$ aerogels and semiconductor properties of TiO$_2$ to significantly yield novel materials appropriate for heterogeneous photocatalysis. When the N atoms get into the skeleton of

TiO$_2$@SiO$_2$ aerogels to form the N-doped TiO$_2$@SiO$_2$ aerogels, a blue shift will appear with N-doped because not only is the top of the TiO$_2$ valence band lowered but the inserted N$_{2p}$ levels are also lower in energy than the valence band of pure TiO$_2$; thus, the N-doped TiO$_2$@SiO$_2$ aerogels have a higher visible light active properties [33]:

$$TiN\,(s) \,+\, O_2\,(g) \longrightarrow TiO_{2-x}Nx\,(s)$$
(2)

$$RhB + TiO_{2-x}Nx@SiO_2 + visible\,light \longrightarrow CO_2 + H_2O$$
(3)

4. Conclusions

To improve the photocatalytic efficiency of TiO$_2$, this work combines the excellent properties of aerogels and nanophotocatalysts to take full advantage of the huge specific surface area, high adsorption efficiency, and strong transmittance of SiO$_2$ aerogel and photocatalytic activity of nanosized N-doped TiO$_2$ simultaneously. Sol-gel method,

supercritical drying, and direct oxidation process were adopted to prepare the nano-N-doped $TiO_2@SiO_2$ ($TiO_{2-x}N_x@SiO_2$, $0 \le x \le 2$) composite aerogels. The specific surface areas of all $TiO_{2-x}N_x@SiO_2$ samples exceeded $700 \text{ m}^2/\text{g}$ and exhibited a honeycomb porous structure with fine particulate morphology. The $500\text{-}TiO_2@SiO_2$ composite aerogel exhibits the best adsorption/photocatalytic degradation rate for RhB, which obtained about 80% of the degradation rate in 30 min under visible light and over 95% after 120 min. Furthermore, as the increase of oxidation temperature, the adsorptivity capacity of $500\text{-}TiO_2@SiO_2$ and $700\text{-}TiO_2@SiO_2$ aerogels is significantly increased after heat treatment because of the improved hydrophilicity of $TiN@SiO_2$ composite aerogel after air treatment. The SiO_2 aerogels can significantly inhibit the phase transition of TiO_2, and the nano-TiO_2 can be highly dispersed in the SiO_2 aerogels. If the oxidation temperature is selected properly, the N-doped $TiO_{2-x}N_x@SiO_2$ aerogel can be obtained by simple oxidation of $TiN@SiO_2$ aerogel.

Data Availability

All data included in this study are available upon request by contact with the corresponding author.

Conflicts of Interest

The authors declare that they have no conflicts of interest.

Acknowledgments

References

[1] M. Qamar and M. Muneer, "A comparative photocatalytic activity of titanium dioxide and zinc oxide by investigating the degradation of vanillin," *Desalination*, vol. 249, no. 2, pp. 535–540, 2009.

[2] V. M. d. S. Rocha, M. d. G. Pereira, L. R. Teles, and M. O. d. G. Souza, "Effect of copper on the photocatalytic activity of semiconductor-based titanium dioxide (anatase) and hematite (α-Fe_2O_3)," *Materials Science and Engineering: B*, vol. 185, pp. 13–20, 2014.

[3] V. Madhavi, P. Kondaiah, and G. Mohan Rao, "Influence of silver nanoparticles on titanium oxide and nitrogen doped titanium oxide thin films for sun light photocatalysis," *Applied Surface Science*, vol. 436, pp. 708–719, 2018.

[4] Y. Ban and X. Wang, "Features and application of titanium dioxide thin films in water treatment," *Procedia Engineering*, vol. 24, no. 3-4, pp. 663–666, 2011.

[5] J. Zhang, Y. H. Wu, F. Xue et al., "Indirect preparation of titanium dioxide oxidation plating layer as photoelectrode used in dye-sensitized solar cells," *Advanced Materials Research*, vol. 953-954, pp. 1095–1098, 2014.

[6] M. Kitano, K. Tsujimaru, and M. Anpo, "Decomposition of water in the separate evolution of hydrogen and oxygen using visible light-responsive TiO_2 thin film photocatalysts: effect of the work function of the substrates on the yield of the reaction," *Applied Catalysis A: General*, vol. 314, no. 2, pp. 179–183, 2006.

[7] J. G. Li, C. C. Tang, D. Li et al., "Monodispersed spherical particles of brookite-type TiO_2: synthesis, characterization, and photocatalytic property," *Journal of the American Ceramic Society*, vol. 87, no. 7, pp. 1358–1361, 2010.

[8] R. Long, Y. Dai, and B. Huang, "Geometric and electronic properties of Sn-doped TiO_2 from first-principles calculations," *The Journal of Physical Chemistry C*, vol. 113, no. 2, pp. 650–653, 2009.

[9] D. Fan, S. Guo, H. Wang et al., "Enhancement of the visible light photocatalytic activity of C-doped TiO_2 nanomaterials prepared by a green synthetic approach," *The Journal of Physical Chemistry C*, vol. 115, no. 27, pp. 13285–13292, 2011.

[10] C. D. Valentin, E. Finazzi, G. Pacchioni et al., "N-doped TiO_2: theory and experiment," *Chemical Physics*, vol. 339, no. 1–3, pp. 44–56, 2007.

[11] M. L. Guo, X. D. Zhang, C. T. Liang et al., "Mechanism of visible photoactivity of F-doped TiO_2," *Chinese Physics Letters*, vol. 27, no. 5, pp. 204–207, 2010.

[12] C. Yan, W. Yi, H. Yuan, X. Wu, and F. Li, "A highly photoactive S, Cu-codoped nano-TiO_2 photocatalyst: synthesis and characterization for enhanced photocatalytic degradation of neutral red," *Environmental Progress & Sustainable Energy*, vol. 33, no. 2, pp. 419–429, 2014.

[13] D. Pang, L. Qiu, Y. Wang, R. Zhu, and F. Ouyang, "Photocatalytic decomposition of acrylonitrile with N-F codoped TiO_2/SiO_2 under simulant solar light irradiation," *Journal of Environmental Sciences*, vol. 33, pp. 169–178, 2015.

[14] C. Zhang, Y. Zhou, J. Bao et al., "Hierarchical honeycomb Br-, N-codoped TiO_2 with enhanced visible-light photocatalytic H_2 production," *ACS Applied Materials & Interfaces*, vol. 10, no. 22, pp. 18796–18804, 2018.

[15] Q. Guo, Z. Zhang, X. Ma et al., "Preparation of N,F-codoped TiO_2 nanoparticles by three different methods and comparison of visible-light photocatalytic performances," *Separation and Purification Technology*, vol. 175, pp. 305–313, 2017.

[16] Y. D. Hou, X. C. Wang, L. Wu et al., "N-Doped SiO_2/TiO_2 mesoporous nanoparticles with enhanced photocatalytic activity under visible-light irradiation," *Chemosphere*, vol. 72, no. 3, pp. 414–421, 2008.

[17] M. Mahato, S. Mukherjee, and T. Mishra, "Development of magnetically separable mesoporous N doped TiO_2-SiO_2 coated Fe_3O_4 nanomaterial as solar photocatalyst for environmental application," *Materials Research Express*, vol. 6, no. 10, Article ID 105544, 2019.

[18] L. Wu, Y. Zhou, W. Nie, L. Song, and P. Chen, "Synthesis of highly monodispersed teardrop-shaped core-shell SiO_2/TiO_2 nanoparticles and their photocatalytic activities," *Applied Surface Science*, vol. 351, pp. 320–326, 2015.

[19] J. Gross, G. Reichenauer, and J. Fricke, "Mechanical properties of SiO_2 aerogels," *Meat Science*, vol. 36, no. 1-2, pp. 203–237, 2000.

[20] C. Sheng, W. Cheng, X. Shen et al., "Mesoporous amine-modified SiO_2 aerogel: a potential CO_2 sorbent," *Energy & Environmental Science*, vol. 4, no. 6, pp. 2070–2074, 2011.

[21] J.-M. Wang, "Preparation and properties of SiO_2 aerogel and fabric composite based on polyurethane," *Integrated Ferroelectrics*, vol. 189, no. 1, pp. 36–43, 2018.

[22] T. Y. Wei, T. F. Chang, S. Y. Lu, and Y.-C. Chang, "Preparation of monolithic silica aerogel of low thermal conductivity by ambient pressure drying," *Journal of the American Ceramic Society*, vol. 90, no. 7, pp. 2003–2007, 2010.

[23] G. Yin, C. Geng, Z. We et al., "Influence of supercritical drying fluids on structures and properties of low-density Cu-doped SiO_2 composite aerogels," *Journal of Sol-Gel Science and Technology*, vol. 69, no. 2, pp. 407–411, 2014.

[24] L. Hu, H. Yuan, L. Zou, F. Chen, and X. Hu, "Adsorption and visible light-driven photocatalytic degradation of Rhodamine B in aqueous solutions by Ag@AgBr/SBA-15," *Applied Surface Science*, vol. 355, pp. 706–715, 2015.

[25] S. Tang, J. Wang, Q. Zhu, Y. Chen, and X. Li, "Oxidation behavior of CVD star-shaped TiN coating in ambient air," *Ceramics International*, vol. 41, no. 8, pp. 9549–9554, 2015.

[26] S. Tang, J. Wang, Q. Zhu, Y. Chen, and X. Li, "Preparation of rutile TiO_2 coating by thermal chemical vapor deposition for anticoking applications," *ACS Applied Materials & Interfaces*, vol. 6, no. 19, pp. 17157–17165, 2014.

[27] Y. N. Kim, G. N. Shao, S. J. Jeon, S. M. Imran, P. B. Sarawade, and H. T. Kim, "Sol-gel synthesis of sodium silicate and titanium oxychloride based TiO_2-SiO_2 aerogels and their photocatalytic property under UV irradiation," *Chemical Engineering Journal*, vol. 231, pp. 502–511, 2013.

[28] X. Huang, J.-X. Liu, F. Shi, L. Yu, and S.-H. Liu, "Ambient pressure drying synthesis of Cs0.33WO3/SiO_2 composite aerogels for efficient removal of Rhodamine B from water," *Materials & Design*, vol. 110, pp. 624–632, 2016.

[29] K. Nakamoto, *Infrared and Raman Spectra of Inorganic and Coordination compounds*, Wiley, New York, NY, USA, fourth edition, 1986.

[30] J. Pan and S. P. Jiang, "Synthesis of nitrogen doped faceted titanium dioxide in pure brookite phase with enhanced visible light photoactivity," *Journal of Colloid and Interface Science*, vol. 469, pp. 25–30, 2016.

[31] S. Livraghi, M. C. Paganini, E. Giamello, A. Selloni, C. Di Valentin, and G. Pacchioni, "Origin of photoactivity of nitrogen-doped titanium dioxide under visible light," *Journal of the American Chemical Society*, vol. 128, no. 49, pp. 15666–15671, 2006.

[32] N. T. Nolan, D. W. Synnott, M. K. Seery, S. J. Hinder, A. Van Wassenhoven, and S. C. Pillai, "Effect of N-doping on the photocatalytic activity of sol-gel TiO_2," *Journal of Hazardous Materials*, vol. 211-212, pp. 88–94, 2012.

[33] G. Barolo, S. Livraghi, M. Chiesa, M. C. Paganini, and E. Giamello, "Mechanism of the photoactivity under visible light of N-doped titanium dioxide. Charge carriers migration in irradiated N-TiO_2 investigated by electron paramagnetic resonance," *The Journal of Physical Chemistry C*, vol. 116, no. 116, pp. 20887–20994, 2012.

[34] S. Yang and G. Lian, "New method to prepare nitrogen-doped titanium dioxide and its photocatalytic activities irradiated by visible light," *Journal of the American Ceramic Society*, vol. 87, no. 9, pp. 1803–1805, 2010.